*Graphical Abstract

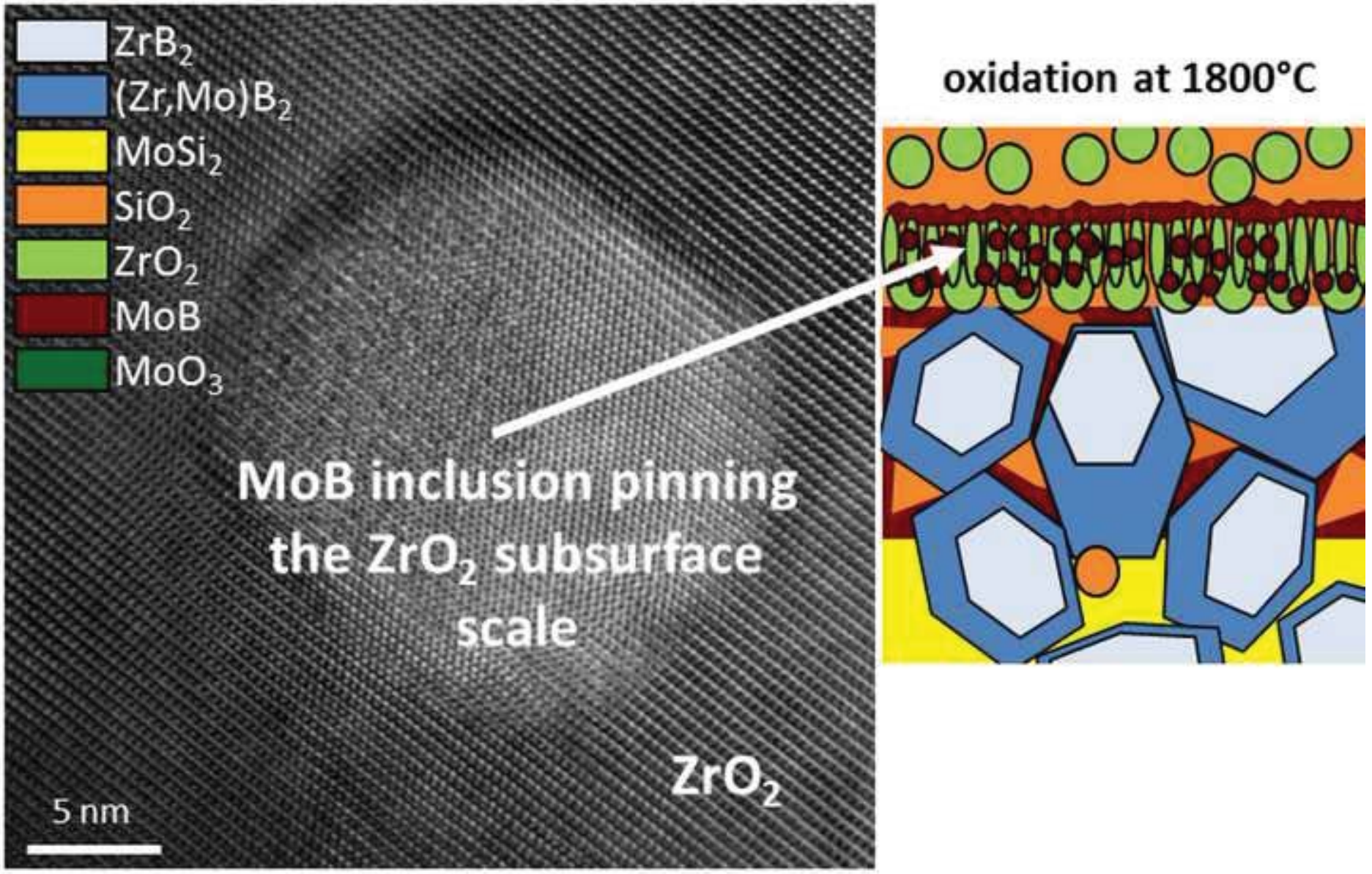

# Understanding the oxidation behavior of a $ZrB_2$–$MoSi_2$ composite at ultra-high temperatures

Laura Silvestroni[1*], Kerstin Stricker[2], Diletta Sciti[1], Hans-Joachim Kleebe[2]

[1]*CNR-ISTEC, National Research Council of Italy - Institute of Science and Technology for Ceramics, Via Granarolo 64, I-48018 Faenza (RA), Italy*

[2]*TU-IAG, Technical University Darmstadt – Institute of Applied Geoscience, Schnittspahnstraße 9, 64287 Darmstadt, Germany*

## ABSTRACT

This basic research investigates the microstructure evolution of a composite based on $ZrB_2$-$MoSi_2$ from the as-sintered features to the changes occurring upon oxidation at ultra-high temperatures, 1650 and 1800°C, in a bottom-up loading furnace for 15 minutes. Scanning and transmission electron microscopy evidenced the formation of a matrix typified by $ZrB_2$-cores surrounded by (Zr,Mo)$B_2$-rims with dispersed $MoSi_2$ particles and $SiO_2$ glass trapped at the triple junctions. The oxidation at 1650°C induced the migration of silica to the surface, which formed a continuous and protective scale. Below this scale, the matrix evolved into $ZrO_2$ grains encasing MoB nano-inclusions, as a result of the oxygen and boron oxide partial pressures established in the subscales. Underneath, a $MoSi_2$-depleted boride region, but substituted by $SiO_2$ and MoB was found. The same phases were observed upon oxidation at 1800°C, but a thicker and more turbulent oxidized layer formed as a consequence of the rapid evolution of $MoO_3$, SiO and $B_2O_3$ gases from the scales beneath the outermost silica-layer.

According to the observed phases and the calculated phase stability diagrams, the partial pressures gradient within the oxide layer were defined and the effect of Mo-doping in boride matrices on the oxidation behavior was compared to that of other transition metals to establish a criterion design for the realization of ceramics with improved oxidation resistance.

**Keywords:** UHTC; Oxidation; TEM; Microstructure; Inclusion.

## 1. Introduction

The great interest in borides and carbides of transition metals, a class of ceramics known as Ultra-High Temperature Ceramics (UHTCs), is motivated by the search for materials that can withstand extreme environments in terms of temperature, chemical reactivity, mechanical stress, radiation and ablation, especially in hypersonic and space aviation [1]. $ZrB_2$ can be considered a leading material in this field of research, due to its unique combination of properties in terms of high melting point above 3000°C, relatively low density, high thermal conductivity and good strength and refractoriness at elevated temperatures [1-5]. However, pure $ZrB_2$ is extremely difficult to sinter, due to its strong covalent bonds and low self-diffusion rates [6] and therefore it requires pressure-assisted sintering techniques at very high

* Corresponding author: Laura Silvestroni
Tel. +39 546 699723
Fax. +39 546 46381
e-mail. laura.silvestroni@istec.cnr.it

temperatures, ~1900°C, to enable the elimination of porosity [7]. Further the $ZrB_2$ powder surface is always covered by oxides, $B_2O_3$ and $ZrO_2$, which lead to an evaporation–condensation mechanism, causing mass transfer without effective densification at low temperatures and exaggerated grain growth at higher temperature, both resulting in poor mechanical properties [7,8].

Another issue of monolithic $ZrB_2$ is its poor oxidation resistance, which results into glassy $B_2O_3$ and crystalline $ZrO_2$ when exposed to air above 800°C [6,9], due to reaction (1):

$$ZrB_2 + 5/2O_2 \rightarrow ZrO_2 + B_2O_3 \quad (1)$$

With rising temperature, above 1100°C, the oxidation protective glassy $B_2O_3$ on top of $ZrO_2$ evaporates leaving a porous $ZrO_2$ scale that, with further temperature increase, undergoes a microstructural transformation from equiaxed to columnar grains, thus letting the oxidation process proceed unhampered [10,11].

Effective approaches to mitigate the sintering issue and simultaneously improve the oxidation resistance of borides foresee the incorporation of secondary phases or additives [7-9, 11-15]. Amongst these, $MoSi_2$ was demonstrated to be one of the most beneficial, able to allow the densification of $ZrB_2$ already at 1750°C, thanks to the formation of a transient liquid phase [16,17], and in particular, to greatly improve the high-temperature mechanical properties and oxidation resistance of $ZrB_2$-based ceramics [16,18-20]. The beneficial effect of $MoSi_2$ during oxidation was ascribed to the formation of glassy $SiO_2$ [13,19] on the outer surface, acting as oxygen diffusion barrier, of stable condensed phases in the subsurface layer such as MoB and $Mo_5Si_3$, and to the suppression of volatile species [13]. The combination of these factors has been suggested as responsible for hindering the evolution of columnar $ZrO_2$ grains in the subsurface, which is detrimental for the fast oxygen diffusion inward into the ceramic matrix [10,15]. The oxidation route of $ZrB_2$ doped with $MoSi_2$ has been indicated as follows [13,19]:

$$ZrB_2 + 5MoSi_2 + 19/2O_2 \rightarrow ZrO_2 + 7SiO_2 + Mo_5Si_3 + B_2O_3 \quad (2)$$

$$2MoSi_2 + B_2O_3 + 5/2O_2 \rightarrow 4SiO_2 + 2MoB \quad (3)$$

Although oxidation mechanisms have been proposed in the middle-high temperature range, 1200-1650°C [13,15], microstructural changes at 1800°C are still unexplored, but fundamental to set a limit temperature which $ZrB_2$-$MoSi_2$ composites can successfully tolerate in aggressive environments. Further, detailed knowledge of chemistry and thermodynamic data of species formed during hot corrosion processes is essential for a better understanding of materials degradation when exposed to high temperature.

In this study, $ZrB_2$ doped with 15 vol% $MoSi_2$ oxidized at 1650°C and 1800°C for 15 min was investigated by transmission electron microscopy (TEM) for the first time. The thorough microstructural

analysis disclosed features at the nano-scale, which were not detectable by other commonly used characterization techniques, such as X-ray diffraction (XRD) or scanning electron microscopy (SEM). Our investigations, coupled with thermodynamic considerations, allowed to shed light on possible phenomena that enable this material to keep good structural integrity even upon oxidation in the ultra-high temperature regime. In addition, we compare the oxidation behaviour of this ceramic to that of other $ZrB_2$-composites containing the same amount of transition metal silicides, $WSi_2$ and $TaSi_2$ [13, 21,22] and propose a design criterion for the realization of even more oxidation resistant composites by introduction of suitable secondary phases.

## 2. Experimental procedure

### 2.1 Materials

15 vol% of $MoSi_2$ was selected as sintering additive for $ZrB_2$ in view of its assessed capability to promote densification during sintering, improve the mechanical properties of the boride [7,8,13,16-18,23] and to provide $SiO_2$ upon oxidation.

The following commercial powders were used: hexagonal $ZrB_2$ (H.C. Starck, Germany, Grade B), specific surface area 1.0 $m^2/g$, impurities (wt%): C: 0.25, O: 2, N: 0.25, Fe: 0.1, Hf: 0.2, particle size range 1.5-3.0 μm and tetragonal $MoSi_2$ (Aldrich, USA), mean grain size 2.8 μm, impurities (wt%) O: 1.

The powders were weighed and mechanically mixed for 24 hours in absolute ethanol using $ZrO_2$ milling media. Subsequently the slurry was dried in a rotary evaporator and sieved through 250 μm screen. A 30 mm-diameter pellet was green shaped by uniaxial pressing at 20 MPa. The pellet was then placed in the furnace and hot pressed in vacuum (~100 Pa), using an induction-heated graphite die with a uniaxial pressure of 30 MPa, the maximum temperature of 1750°C and a dwell time of 20 minutes were set on the basis of the shrinkage curve, free cooling followed.

### 2.2 Oxidation methods

The resistance to oxidation was studied using a bottom-loading furnace (Nannetti FC18, Faenza, Italy) exposing a rectangular coupon 13.0 x 2.5 x 2 $mm^3$ for 15 minutes to the effect of stagnant air at 1650 and 1800°C. The coupons, previously cleaned in acetone and weighed, were placed on $ZrO_2$ supports and bottom-up loaded into the hot zone of the furnace when the target temperature was reached, elapsed 15 minutes and rapidly cooled down to allow air-quenching.

### 2.3 Characterization and Computations

Crystalline phases of the oxidized ceramics were identified by X-ray diffraction (XRD, mod. D8 Advance - Bruker, Germany) with Cu Kα radiation, step size of 0.02 and 0.5 s counting rate in the 20-130°C 2-Theta range.

The microstructure before and after oxidation was analyzed on fractured and polished cross sections by field-emission scanning electron microscopy (FESEM, mod. ΣIGMA, ZEISS NTS GmbH, Germany) coupled to an energy dispersive X-ray micro-analyzer (EDS, mod. INCA Energy 300, Oxford Instruments, UK).

The samples for TEM analyses were prepared cutting a disc from the as-sintered pellet and from the oxidized coupons. The discs were mechanically ground down to about 20 μm and then further ion beam thinned until incipient perforations were observed by optical microscopy. Local phase analysis was performed using a transmission electron microscope (TEM, JEOL JEM 2100F, Tokyo, Japan) operating at a nominal voltage of 200 kV and being equipped with an energy-dispersive X-ray system (EDS, mod. INCA Energy 300, Oxford Instruments, UK). Electron diffraction pattern identification was carried out through the software tool developed for Digital Micrograph [24].

Key microstructural features like mean grain size and volumetric content of the secondary phases were evaluated from FESEM micrographs elaborated with the support of the commercial software package Image Pro Plus (v.7, Media Cybernetics, USA).

Thermodynamics and phase stability diagrams were computed by means of the commercial package HSC Chemistry v. 6.1 (Outokumpu Research Oy, Pori, Finland).

## 3. Results

### 3.1 As-sintered microstructure

The as-sintered microstructure of this ceramic has been already extensively described in previous works [7,8,13,16-18,23], but the main characteristics are summarized in Table I for the sake of clarity.

$ZrB_2$ appears as rounded grains, around 2.4 μm, Fig. 1a, and shows a substructure called "core-rim" structure, Fig. 1b. The core is the original $ZrB_2$ nucleus, while the rim is an epitaxial $(Zr,Mo)B_2$ solid solution, with a Mo content of around 5 at%, Fig. 1c-f. TEM analysis further revealed the presence of dislocations in the rim, whereas the core and adjacent $MoSi_2$ grains are dislocation-free, Fig. 1c-d. In some cases, rounded $SiO_2$ inclusions are found trapped at the core/rim interface, Fig. 1g. Such kind of inclusions, based on $SiO_2$-SiC, have been reported for analogous systems [25]. The formation of core-rim structures is not new and has already been reported in previous studies [17,18]. The most plausible hypothesis to explain its formation relies on a dissolution-precipitation mechanism assisted by a transient liquid phase formed during sintering that enhances mass transfer [17,23].

$MoSi_2$ has a irregular shape with convex contours, filling residual intersitials within the $ZrB_2$ skeleton; its size varies between 1 and 3 μm.

The boride-$MoSi_2$ skeleton is interrupted by $SiO_2$ pockets in which crystalline $ZrO_2$ precipitated, Fig. 2. In addition, less than 1 vol% of MoB phase is found, often located as apical tips of $MoSi_2$. Its formation is presumed to be a consequence of the interaction between the oxide phases covering the starting particles, $MoO_3$ and $B_2O_3$, during the sintering process [23].

### 3.2 Microstructure upon oxidation

**1650°C -** XRD analysis performed on the oxidized surface, Fig. 3a, evidences that the main crystalline phase is monoclinic $ZrO_2$, but $ZrB_2$ reflections remain visible in traces even after oxidation at this temperature for 15 min, indicating a thin oxide layer. $MoSi_2$ peaks disappeared leaving the tetragonal MoB phase instead. No clear $Mo_5Si_3$ phase can be identified.

Images of the microstructure of the composite oxidized at 1650°C are displayed in Fig. 4-6. The surface consists of a continous glassy $SiO_2$ layer. On the top of it, isolated $ZrO_2$ aggregates with smooth contours, indicating a low wettability, are commonly found, Fig. 4a-c.

An overview of the polished cross section reveals a three layered structure, Fig. 5, and EDS mapping evidences the elemental distribution. The full oxidation scale is approximately 60-70 µm in thickness. In layer I, a compact glassy $SiO_2$ layer, of approximately 15 µm thickness, comprises agglomerates and droplet shaped $ZrO_2$ with dispersed Mo/B particles, Fig. 5. Right underneath, layer II, an accumulation of the MoB phase is found, standing on a 50 µm thick layer of modified material where $SiO_2$ and MoB replaces $MoSi_2$ within the boride matrix. Then the unoxidized bulk starts.

TEM analysis in layer I evidenced that $ZrO_2$ grains display a peculiar arrangement with inclusions of nano-sized MoB which partially distorted $ZrO_2$ lamellae, Fig. 6. No orientation relationship between the MoB precipitates and the surrounding $ZrO_2$ can be identified. The formation of such intra-granular structure in the subsurface layer has previously been observed upon oxidation of $ZrB_2$ doped with other transition metals, Me, like W and Ta, and it has been proposed to be a typical feature of the oxidized starting $(Zr,Me)B_2$ solid solution [21,22].

At the layer I/layer II interface, silica accumulation is found in correspondence of bumps in the upstanding $ZrO_2$ aggregates, Fig. 5.

Moving inwards to layer II, a sharp transition occurs in terms of change of type, shape and amount of the major phases: the original $ZrB_2$-$MoSi_2$ skeleton does not exist anymore. Instead, a network of adjacent $SiO_2$ and MoB penetrates the boride matrix, Fig. 7a. MoB is characterized by irregular 2-5 µm grains and smooth appearance with no dislocations, Fig. 7b,c. $SiO_2$, with dark contrast in SEM images and containing $ZrO_2$ precipitates, is present in increased amount with respect to the bulk. TEM analysis further evidenced an amorphous $MoO_x$ phase, filling the matrix interstitials in the upper zone of layer II, Fig. 7d-f. A possible stoichiometry could be $MoO_3$, which is the most favorable species with respect to the possible oxidation states, as discussed later. Its existence could be explained by condensation of a gaseous phase upon rapid cooling. Further, its formation at the grain boundaries and triple junctions can be attributed to a limited solubility of Mo in silicate and borosilicate glasses [26]. Similarly, in oxidized $ZrB_2$-$WSi_2$ composites, a $WO_3$ phase was found [21].

The bulk microstructural features remained basically unchanged as compared to the as-sintered microstructure described above.

**1800°C –** XRD analysis revealed that upon oxidation at 1800°C, besides monoclinic $ZrO_2$ and tetragonal MoB, peaks corresponding to silica are also possibly present, Fig. 3b, similar to what has been observed upon oxidation of $ZrB_2$-SiC composites between 1700 and 1900°C [27]. The presence of the peak at $2\theta=23°$, absent instead upon oxidation at 1650°C, is possibly due to the favorable active oxidation of $SiO_2$ to volatile SiO at high temperature and to its precipitation upon air quenching.

The surface of the specimen still presents a glassy scale with some large bubbles, inset in Fig. 4d, which leaves exposed $ZrO_2$ grains with dendritic shape or decorated with Mo-B features, Fig. 4d-e. SEM-EDS inspection revealed silica glass in the dark areas and zirconia where the bubble burst. At the glass–zirconia interface beneath the bubble, $MoO_3$ grains in platelet shape and $SiO_2$ whiskers formed as a consequence of vapor phases reactions, Fig. 4f. [28].

An overall view of the oxidized cross section with elemental mapping evidenced four different layers with a fully oxidized thickness of approximately 180 µm, Fig. 8. In contrast to the sample oxidized at 1650°C, the layers appear more turbulent, with some cavities and bubbling, indicating possible liquid and vigorous gas formation at such high temperature. Noteworthy is also the accumulation of Mo-B phase at layer I/layer II interface and the corresponding Mo-impoverishment in layer III. Also Si displays an inhomogeneous distribution across the section: below the outermost $SiO_2$ scale in layer I, it is mainly concentrated at the layer II/layer III interface, where accumulation of possibly $MoO_x$ is presented.

The outermost scale, layer I, about 50 µm thick, is composed of compact $ZrO_2$ and silica. Small bright precipitates and coarser aggregates are homogeneously distributed in the $SiO_2$ glass, Fig. 9a,b. TEM images confirm that these re-precipitations appear clustered and show a characteristic twinned lamella structure, typical of the martensitic $ZrO_2$ transformation [29], Fig. 9c,d. Amongst these clusters, boron, iron and calcium are found as well, see inset in Fig. 9c. $ZrO_2$ at the MoB/$SiO_2$ interface is characterized by a dendritic-like crystallization, Fig. 9b. The detection of boron at 1800°C, in particular so close to the surface could be due to variations of the glass properties, which allow for a greater dissolution of cations, constituting a denser and more viscous barrier, thereby decreasing the evaporation rate of $B_2O_3$ [30]. In addition, along the edges of coarser $ZrO_2$ grains, an impoverishment of $ZrO_2$ precipitates is usually observed, indicating a coarsening process. The same phenomenon is observed at the layer I/layer II interface, Fig. 9b.

Layer II is topped by a continuous ribbon of MoB aggregates with visible cracks, Fig. 9a, which is located on columnar $ZrO_2$ crossed by a silico-borate glass, Fig. 10a-c. The columnar $ZrO_2$ grains are approximately 2-5 µm wide and have a length between 10-20 µm. The columns are densely packed and adapt their shape in conjunction to each other. At their base, a globular $ZrO_2$ type is found, indicating a

variation of gas pressure at this interface. Again, rounded MoB aggregates with increased size up to 100 nm are embedded within both types of $ZrO_2$ grains. Small cracks originate from these inclusions, Fig. 10b-d. Inclusions with darker contrast indicated in Fig. 10d contain also Ti, with (Mo,Ti)B as possible formula. These are supposed to be impurities collected during powder processing.

Moving to layer III, a 45 µm scale looks more damaged due to grain pullout during the polishing procedure. This scale is $MoSi_2$-depleted, whilst $ZrB_2$, MoB and $SiO_2$ are the dominant phases with $SiO_2$ forming an interconnected network. This layer has the same features as layer II in the sample oxidized at 1650°C, presented in Fig. 7.

Analysis of the bulk indicates a grain shape homogenization as compared to the as-sintered microstructure. All $ZrB_2$, $MoSi_2$ phases show idiomorphic hexagonal grains with sharp and straight boundaries, Fig. 11. It is possible that the oxidation temperature of 1800°C, higher than the sintering one of 1750°C, favors grains rearrangement and the establishment of low energy grain configurations.

## 4 Discussion

In order to visualize the microstructure evolution that occurred from the as-sintering state up to oxidation at 1650 and 1800°C, the simplified sketch in Fig. 12 will be used in conjunction with the summary of the most important features and phases formed in the various layers upon oxidation, as reported in Table I.

### 4.1 Phases stability domain and oxidation behavior

The oxidation of this system is defined by oxygen inward diffusion through the sample and the outward diffusion of Si, B and Mo towards the sample surface, as cleary recognizeable by looking at the elemental mapping across the sections of the oxidized ceramics in Figs. 5 and 8.

Initially, $ZrB_2$–$MoSi_2$ ceramic consists of a $ZrB_2$ matrix with dispersed $MoSi_2$ and $SiO_2$ particles. A $(Zr,Mo)B_2$ solid solution is also present around the original $ZrB_2$ grains, due to partial silicide decomposition in reducing environment during the consolidation process, Fig. 12a.

When exposed to air and in the temperature range considered here, $ZrB_2$ and $MoSi_2$ equally tend to oxidize following reactions (1) and (4)[†]. Therefore, the oxidation of $MoSi_2$ will yield an oxide layer that consists of a continuous silica glass and $MoO_3$ and the $ZrB_2$ will produce crystalline $ZrO_2$ and liquid $B_2O_3$. If we consider the specific oxidation of the boride solid solution, reaction (5) is proposed:

$$ZrB_2 + 5/2O_2 \rightarrow ZrO_2 + B_2O_3 \quad (1)$$

$$MoSi_2 + 7/2O_{2(g)} \rightarrow 2SiO_2 + MoO_{3(g)} \quad (4)$$

$$(Zr_{1-x}Mo_x)B_2 + (5/2-7x/4)O_{2(g)} \rightarrow (1-x)ZrO_2 + xMoB + (1-x/2)B_2O_{3(l/g)} \quad (5)$$

[†] The free Gibbs energy, $\Delta G$, normalized for the moles of oxygen for reactions 1 and 4 at 1650°C is -123 and -130 kcal, respectively and at 1800°C is -85 and -84 kcal, respectively.

Owing to its high vapor pressure, $B_2O_{3(l)}$ readily evaporates resulting in a $B_2O_3$ gradual impoverishment of the liquid glass from the surface down to the solid structure [31]. Similarly, Mo-oxides are highly volatile already below 1000°C [32], so that at 1650°C, both $B_2O_3$ and $MoO_3$ immediately leave the system if they are located on the outermost surface leaving a pure silica top layer. Silica has very low diffusivity for oxygen and is a very protective scale at high temperatures. Active oxidation of $SiO_2$ to gaseous SiO is reported to occur above approximately 1800°C [33]. On the contrary, across the $ZrO_2$–$SiO_2$ sub-layers, small fractions of $B_2O_3$ remain dissolved in the glass, in agreement with our findings, see the EDS spectrum in Fig. 10, and previous studies on B-retention within the $SiO_2$-glass [34].

The initially formed $ZrO_2$ remains concentrated near the surface, forming a two-phase $ZrO_2$–$SiO_2$ layer with stable MoB nano-inclusions interpenetrating $ZrO_2$ grains, and beneath $MoSi_2$ continues to oxidize in presence of $B_2O_3$ resulting in a $SiO_2$ and MoB network within the boride matrix, Fig. 12b. Therefore, the overall oxidation mechanism of the composite can be described by reactions (1, 3-7):

$$2MoSi_2 + B_2O_3 + 5/2O_2 \rightarrow 4SiO_2 + 2MoB \quad (3)$$

$$ZrB_2 + MoSi_2 + 6O_{2(g)} \rightarrow ZrO_2 + 2SiO_{2(l)} + MoO_{3(g)} + B_2O_{3(g)} \quad (6)$$

$$2MoB + 9/2O_{2(g)} \rightarrow 2MoO_{3(g)} + B_2O_{3(g)} \quad (7)$$

where (1), (4)-(7) describe events occurring on the surface, whilst (3) is explicative of phenomena occurring in the sub-surface.

The formation of these oxidation products has been verified via SEM and TEM measurements in both oxidation regimes, implying that the overall oxidation mechanism from high to ultra-high temperature does in principle not change. However, in chemically controlled reactions, pressure has an important effect on the rate of oxidation. What dramatically changes is therefore the oxidation kinetics, in turn influenced by development of gases at the various temperatures which induce variations of the partial pressures in the subsurface scales. Given the lack of kinetic data for the corrosion processes, an alternative approach to understand the thermodynamic behavior of chemical species is to utilize phase stability diagrams. In addition, an increase of the temperature, and thereby the reaction rates, causes diagrams solely based on thermodynamic considerations to be more relevant [35].

The oxygen partial pressure ($pO_2$) underneath the outermost scale is significantly lower than at ambient atmosphere ($pO_2$ = 0.2 atm), due to the chemical potential gradient associated with the diffusion profile. A precise definition of the pressure in the sub-scale layers is difficult, however we can provide pressure ranges by comparing the condensed phases experimentally observed in the sublayers and the phase stability diagrams calculated at fixed temperatures varying the partial pressure of the two main gases: $O_2$, penetrating through the ceramic, and the upstreaming $B_2O_3$, largely developed by oxidation of the matrix [36]. Fig. 12b,c plot the most stable phases for the Zr-B-O (black line) and Mo-B-O (red line) systems as a function of the partial pressures at 1650°C and 1800°C, with an estimation of the pressure

intervals in the sketch aside. It can be noticed that increasing the oxidation temperature, the stability field of non-oxides increases given the exothermic nature of the oxidation reaction.

Based on experimental observations, in layer I at 1650°C, $ZrB_2$ is completely oxidized to $ZrO_2$ and this enables to preserve un-oxidized MoB inclusions within the grains under the conditions of pressures defined by the blue area in Fig. 12b. In the same layer, in the material oxidized at 1800°C, MoB inclusions are hardly found, indicating continuous $MoO_3$ evaporation, thus possible pressure conditions are marked in blue in the plot of Fig. 12c. The oxygen activity in layer II at 1650°C, or in layer III at 1800°C is low enough to prevent oxidation of $ZrB_2$ as it remains un-oxidized and the limited $B_2O_3$ available is captured by the oxidizing $MoSi_2$ to form MoB, with estimated pressure conditions marked in green in the plots of Fig. 12b,c.

A situation observed just upon oxidation at 1800°C is the formation of columnar $ZrO_2$, confined in layer II in Fig. 12c and defined by the pressure conditions highlighted in grey in the plot aside.

Looking at Fig. 10a,b, a variation of $ZrO_2$ coarsening from globular to columnar testifies a critical variation of partial pressure at this interface. The formation of columnar $ZrO_2$ has been reported upon oxidation of pure borides above 1000°C [10], of $ZrB_2$-SiC composites above 1650°C [12,27 37] and, more generally, for all boride-based ceramics starting at 1600°C, including those doped with different transition metals [13,21,22,30]. The observed columnar growth of $ZrO_2$ grains develop starting from the originally equiaxed $ZrO_2$ particles which act as growth sites for $ZrO_2$ precipitating from the receding glass [30]. This morphology change indicates an accelerated coarsening in a preferred growth direction, which is commonly attributed to the evolution of gaseous by-products and the rapid flow of liquids [10,36]. In this case, liquid phases cause convection phenomena which make zirconia grow in the form of columns, as a consequence of the fast transport of low the viscosity boro-silicate phase.

### 4.3 Effect of Mo on the oxidation behavior at ultra-high temperature

Remarkably, the addition of $MoSi_2$ retards the formation of columnar $ZrO_2$, as this morphology appears at higher temperatures as compared to other $ZrB_2$-systems, especially $ZrB_2$-SiC systems [13]. Possible reasons could be related to the consumption of of $B_2O_3$ content in the subsurface liquid through reaction with $MoSi_2$ to form solid MoB, reactions (3,5), as observed in Fig. 9a, with accumulation of MoB in a ribbon shape. Indeed, the reduction of $B_2O_3$ amount in the glass could result in increased viscosity compared to the usual boro-silicate glass of $ZrB_2$-SiC systems, where the formation of columnar $ZrO_2$ is systematically observed. In addition, the dissolution of a small amount of Mo into the silica scale, which is actually reported to act as a reticulating agent in glass structures [26], could further change and increase the viscosity of the liquid phase, thus acting as an effective barrier against oxygen inward diffusion. No Mo was detected by EDS within the silica-glass running through $ZrO_2$ columnar grains; however, amorphous $MoO_3$ was found in the $MoSi_2$-depleted region, Fig. 7d-f, indicating some Mo solubility within the silico-borate glass and phase separation upon quenching.

On the other hand, the pronounced bubbling activity observed on the surface of the oxidized sample at 1800°C, Fig. 4d, indicates the formation of localized gaseous species in the subsurface layers. The fact that $SiO_2$ whiskers and $MoO_3$ platelets were found at the basis of the burst glass bubbles on the sample surface with morphology typical of growth assisted by a vapor phase, Fig. 4f, lead to the conclusion that the evolution of gaseous SiO and $MoO_x$ is very rapid at this temperature.

The microstructure analysis of this compound showed that Mo-phases close to the surface are found mainly as MoB, but occurring in two morphologies, depending on the oxidation temperature experienced: upon 1650°C it is mostly homogeneously spread and encased as nano-inclusions within zirconia grains, Fig. 3, upon 1800°C it forms a continuous 5 µm thick cordillera, Fig. 9a. The gas pressure released once oxygen reaches each MoB typology changes according to its size and distribution, i.e. higher amount of $MoO_3$ will be released in correspondence of large particles, especially because it is reported to vaporize accompanied by "important gas turbulence" [32]. This effect can be better appreciated looking at the elemental maps in Fig. 5: if we follow the profile of the $ZrO_2$ bumps created in layer I, we can see that the layer II directly beneath is Mo-impoverished, indicating a preferential Mo migration upwards and vaporization.

Considering the microstructure upon oxidation at 1800°C, two pressure thresholds define layer II: on the bottom, a change of gas evolution is recorded, as indicated by the development of columnar $ZrO_2$; on the top, another abrupt variation make $MoO_x$ and $B_2O_3$ recombine to form a continuous band of MoB. This phase accumulation close to the surface is supposed to be the main responsible for the development of high amount of localized $MoO_3$ which provokes bursting in the silica glass and $ZrO_2$ lifting, Fig. 8.

In a nutshell, considering the supply of Mo-phases in future ceramics, it would be preferred to have a homogenously distributed source, i.e. a continuous $(Zr,Mo)B_2$ solid solution without discrete large Mo-phases. This hypothesis has been confirmed in a recent specific study [38].

### 4.4 Criterion design for UHTCs with improved oxidation resistance

This and previous SEM and TEM analyses [21,22] demonstrated that it is essential to raise more awareness on the complex microstructure change of $ZrB_2$ doped with transition metals, Me= Mo, W and Ta, and their behavior upon oxidation. Besides, the evolution of the $(Zr,Me)B_2$ solid solution, present in all as-sintered $ZrB_2$-$MeSi_2$ composites, to a new morphology in the sub-surface layer where $ZrO_2$ encases homogeneously dispersed nano-inclusions containing the guest cation in various chemistry has been ascertained. Therefore, in this paragraph we will try to outline the main factors that should be considered during compositional design of new UHTCs possessing further improved oxidation performances. The matters addressed here concern phenomena that can enhance the oxidation behavior and occur either on the outer surface (oxide melting or densification, phase separation) or in the subsurface scale (development of a compact dense layer).

Table II summarizes microstructural features detected in the various $ZrB_2$-$MeSi_2$ compounds and the available crystalline and physical properties of relevant compounds [21,22].

As first remark, we have seen that upon sintering, the **amount of Me dissolved** in the $ZrB_2$ lattice, resulting in the core-rim substructure, varies depending on the atomic radius of the cation: Me with atomic radius more similar to that of Zr preferentially substitutes it in $ZrB_2$, i.e. more Ta can enter than Mo and W. In addition, considering just one type of Me, its amount can be slightly increased by processing the material at higher sintering temperatures, for example in the case of Mo, when the densification temperature is set at 1900°C, the resulting solid solution contains a lower amount of Mo than one obtained at 2150°C, 6 and 12 at%, respectively [38].

A direct consequence of this regards the **volume fraction** of nano-inclusions formed upon oxidation, which is primarly related to the amount of cation dissolved in the solid solution according to the stoichiometries proposed in reactions (8-10):

$$(Zr_{0.95}Mo_{0.05})B_2 + 4.825O_{2(g)} \rightarrow 0.95ZrO_2 + 0.05MoB + 0.975B_2O_3 \quad (8)$$

$$(Zr_{0.80}Ta_{0.20})B_2 + 2O_2(g) \rightarrow 0.80ZrO_2 + 0.20TaB_2 + 0.80B_2O_3 \quad (9)$$

$$(Zr_{0.98}W_{0.02})B_2 + 4.96O_2(g) \rightarrow 0.98ZrO_2 + 0.02W + B_2O_3 \quad (10)$$

These inclusions in turn have a different grain size, 15-20 nm for Mo and W doping, 140 nm for Ta, but at present no plausible explanation can be provided to explain these size variations. Accordingly, the spatial **distribution** of such inclusions is strictly related to both volume fraction and size.

The second important difference concerns the **nature** of the nano-inclusions trapped within $ZrO_2$ grains that form upon oxidation: depending on the oxygen and boron oxide partial pressures established in the growing oxide, the formation of diborides, monoborides or pure metal is more favorable, i.e. MoB, $TaB_2$ or W [21,22].

Volume fraction, size, distribution and nature of such particles impact on the **stress state of $ZrO_2$** grains in which they are dispersed, owing to the coupling of different phases with different thermo-elastic properties. To have an estimate of the stresses in the $ZrO_2$ grains and layer as a consequence of the dispersed nano-inclusions, we employed Taya's model using the relationships described in Appendix 1 as Supplementary Information with input values reported in Table II [39]. The result is a compressive stress state in the particles, $\sigma_p$, and a corresponding tensile stress state in $ZrO_2$ grains, $\sigma_m$. Despite differences in the properties of the inclusions, the predicted residual tensile stress in $ZrO_2$ is in the same order of magnitude, 24-32 MPa.

Assessed this similar stress state in the zirconia scale, what looks more important with respect to the oxidation advancement in the subsurface layer is what is going to happen when oxygen reaches such

intragranular nano-structure. Each type of inclusion is destined to oxidize into the most **favorable oxide**, i.e. $MoO_3$, $WO_3$ and $Ta_2O_5$, and the way this transformation occurs is crucial.

It is reported that the vaporization of $MoO_3$ and $WO_3$ occurs instantly already at much lower temperatures than the one considered here [40]. Therefore, these two compounds will either develop a gas phase in the subsurface scale, possibly resulting in uplifts of the outer scale, or immediately leave the system if they are located close to the outermost surface. Pure $Ta_2O_5$ can be seen as a refractory compound with a melting point of 1872°C, but unfortunately in such type of ceramics we are never in presence of a single phase. As such, eutectic melts are foreseen already above 1550°C [41] and evaporation of Ta-sub-oxides occurs at temperatures exceeding 1600°C [42]. Hence, tantalum oxides present on the surface will not be able to effectively protect from oxygen diffusion in the ultra-high temperature regime [13,21,22]. In addition, the transition from Ta-boride to Ta-pentoxide is accompanied by a large volume expansion that proved to be catastrophic for the disruption of the $ZrO_2$ scale [22].

Previous investigations evidenced that beneficial effects of Me dissolved in the outermost layer by reducing oxygen transport and delaying oxidation are appreciable up to 1400-1600°C: Ta and Cr were identified as the most efficient in promoting phase separation by increasing cation field strength and induce glass immiscibility [43], while Mo and Nb are the most capable to increase the stability of the protective liquid/glassy layer due to a lower evaporation rate for $B_2O_3$ glasses [30]. However, in view of the high oxides volatility at ultra-high temperatures or in ablative environments, compositional variations of the outer glass are supposed to play a minor role in retarding material consumption. Thus, major attention should be paid on the possibility of tailoring the sub-surface layer.

What emerges from these considerations is that the choice of cation to be dissolved into the boride matrix has a paramount importance. As long as the nano-inclusions nestled within $ZrO_2$ are located at oxygen partial pressure below $10^{-10}$-$10^{-12}$ Pa, they are stable as solid compounds. So, one design criterion for the realization of oxidation resistant ceramics should focus on the introduction of dopants, able to form a $(Zr,Me)B_2$ solid solution with the highest stability field in the region of highest oxygen partial pressure. To identify the most suitable Me candidates, predominance diagrams were computed at 1650°C for several systems including Me from the 3$^{rd}$ to the 7$^{th}$ group including La-B-O, Ti-B-O, Hf-B-O, Nb-B-O, Ta-B-O, Cr-B-O, W-B-O and Re-B-O, besides Zr/Mo-B-O already presented in Fig. 12. The predicted nature of the nano-inclusions in the sub-surface scale with $PO_2$ below $10^{-13}$ atm and $PB_2O_3$ below $10^{-2}$ atm, calculated with HSC Chemistry software, is reported in Fig. 13b and the single plots are available as Supplementary Information in Fig. S1. These plots confirm that Mo, Cr and W have stability field at the highest oxygen partial pressures, supporting Kazmedashi et al. [30] and Talmy et al.'s [43] experimental findings. Particularly worth to mention is that Re is predicted to oxidize only at very high $PO_2$, above $10^{-3}$ atm, and could therefore be a good candidate for ultimately improve the oxidation resistance of $ZrB_2$.

## 5. Conclusions

The microstructure evolution of a $ZrB_2$ – 15 vol% $MoSi_2$ ceramic was investigated by means of scanning and transition electron microscopy from the as-sintered state up to its appearance upon oxidation in the ultra-high temperature regime, 1650 and 1800°C for 15 min.

The as-sintered boride matrix displays a typical "core-rim" grain structure, where the core is $ZrB_2$ and the rim a $(Zr,Mo)B_2$ solid solution. The main secondary phase is $MoSi_2$ with minor amounts of $SiO_2$, SiC and MoB, formed as a consequence of the silicide dissociation and reaction with the reducing atmosphere during the consolidation process.

The oxidation resistance in a bottom-up loading furnace at 1650°C for 15 minutes generated a multilayered oxidized architecture with an outermost $SiO_2$-$ZrO_2$ scale. The distinctive feature of the $ZrO_2$ grains was the formation of an intra-granular structure where MoB nano-inclusions were homogeneously dispersed and nestled within $ZrO_2$. Underneath, a $MoSi_2$-depleted diboride skeleton was found, where the silicide sites were occupied by adjacent $SiO_2$ and MoB phase.

An increase of the oxidation temperature to 1800°C almost tripled the thickness of the oxidized scale, from 60-70 µm to 180 µm, being however the thinnest oxidize scale ever formed in such conditions in $ZrB_2$-ceramics doped with various transition metals, generally in the order of 200-390 µm at 1650 and 1800°C, respectively. The conditions for the formation of columnar $ZrO_2$ grains, normally observed in $ZrB_2$-SiC composites already upon oxidation at 1650°C, were achieved only upon oxidation at 1800°C, due to a variation of the gases partial pressure established by the introduction of Mo in this system.

This study pointed out the beneficial effect of the solid solution structure, which guarantees a diffused Mo supply thus limiting turbulence and bursting phenomena on the surface, due to the evolution of volatile Mo-oxides, as compared to discrete and coarser Mo-based phases.

Lastly, a comparative computation on the oxidation behavior of $ZrB_2$ doped with various transition metals revealed that one of the design criteria for the realization of highly oxidation resistant materials is to select dopants with the largest stability domain at high oxygen partial pressure, which were identified to be Mo, Cr, W with Re being the most suitable.

**Acknowledgements**

Part of this study was carried out in the frame of the project "Development of novel buffer layers", n°KL615 29-1, funded by the German Science Foundation (DFG). Part of the research leading to these results has received funding from the European Community's Horizon 2020 "Research and innovation programme" under grant agreement C3HARME No. 685594.

**References**

1) E. Wuchina, E. Opila, M. Opeka, W.G. Fahrenholtz, I. Talmy, UHTCs: ultra-high temperature ceramic materials for extreme environment applications, Electrochem. Soc. Interf. 16 (2007) 30–36.

2) D.M. Van Wie, J.R. Drewery, D.E. King, C.M. Hudson, The hypersonic environment: Required operating conditions and design challenges, J. Mater. Sci. 39 (2004) 5915-5924.
3) F.Monteverde, A.Bellosi, S.Guicciardi, Processing and properties of zirconium diboride-based composites. J. Eur. Ceram. Soc. 22 (2002) 279-288.
4) A. L. Chamberlain, W.G. Fahrenholtz, G. E. Hilmas, D.T. Ellerby, High strength $ZrB_2$-based ceramics. J. Am. Ceram. Soc. 87 (2004) 1170-1172.
5) M. M. Opeka, I. G. Talmy, J. A. Zaykoski, Oxidation-Based Materials Selection for 2000°C Hypersonic Aerosurfaces: Theoretical Considerations and Historical Experience. J. Mater. Sci. 39 (2004) 5887–5904.
6) J.K. Sonber, A.K. Suri, Sythesis and consolidation of zirconium diboride: Review. Adv. Apl. Ceram., 10 (2011) 321-334.
7) W.G. Fahrenholtz, G.E. Hilmas, I. Talmy, J.A. Zaykoski, Refractory Diborides of Zirconium and Hafnium, J Amer. Ceram. Soc. 90 (2007) 1347-1364.
8) S.-Q. Guo, Densification of $ZrB_2$-based composites and their mechanical and physical properties: A review, J. Europ. Ceram. Soc. 29 (2009) 995-1011.
9) F.Monteverde, A.Bellosi, Oxidation of $ZrB_2$-Based Ceramics in Dry Air, J. Electrochem. Soc. 150 (2003) B552-B559.
10) T.A.Parthasarathy, R.A. Rapp, M. Opeka, R.J. Kerans, A model for the oxidation of $ZrB_2$, $HfB_2$ and $TiB_2$, Acta Mater. 55 (2007) 5999-6010.
11) W.C.Tripp, H.C. Graham, Thermogravimetric Study of the Oxidation of $ZrB_2$ in the Temperature Range of 800° to 1500°C, J. Electrochem. Soc. 118 (1971) 1195-1999.
12) I.G. Talmy, M.M. Opeka, S. Dallek, Oxidation of $ZrB_2$ ceramics modified with SiC and Group IV-VI Transition Metal Diborides, Electrochem. Soc. Proc. 12 (2001) 144-158.
13) L. Silvestroni, G.Meriggi, D.Sciti, Oxidation behavior of $ZrB_2$ composites doped with various transition metal silicides, Corr. Sci. 83 (2014) 281-291.
14) A.D. Panasyk, O.N. Grigoriev, A.V. Koroteev, Interaction between $ZrB_2$-$MoSi_2$ Cermets and Oxide Melts, Powder Metall. Met. Ceram. 53 (2014) 330-334.
15) P. Hu, X.-H. Zhang, J.C. Han, X.-G. Luo, S.-Y. Du, Effect of Various Additives on the Oxidation Behavior of $ZrB_2$-Based Ultra-High Temperature Ceramics at 1800°C, J. Am. Soc. 93 (2010) 345-349.
16) D. Sciti, F. Monteverde, S. Guicciardi, G. Pezzotti, A. Bellosi, Microstructure and mechanical properties of $ZrB_2$-$MoSi_2$ ceramic composites produced by different sintering techniques, Mat. Sci. Eng. A 434 (2006) 3003-3009.
17) L. Silvestroni, H-J. Kleebe, S. Lauterbach, M. Müller, D. Sciti, Transmission Electron Microscopy on Zr- and Hf-borides with $MoSi_2$ addition: Densification Mechanisms, J. of Mater. Res. 25 (2010) 828-834.
18) L. Silvestroni, D. Sciti, Effects of $MoSi_2$ additions on the properties of Hf- and Zr-$B_2$ composites produced by pressureless sintering, Scripta Mater. 57 (2007) 165-168.
19) D. Sciti, M. Brach, A. Bellosi, Long-term oxidation behavior and mechanical strength degradation of pressurelessly sintered $ZrB_2$-$MoSi_2$ ceramic, Scr. Mater. 53 (2005) 1297-1302.
20) S.-Q. Guo, T. Mizuguchi, T. Aoyagi, T. Kimura, Y. Kagawa, Quantitative Electron Microprobe Characterizations of Oxidized $ZrB_2$ Containing $MoSi_2$ Additives, Oxid. Met. 72 (2009) 335-345.
21) L. Silvestroni, D. Sciti, F. Monteverde, K. Stricker, H.-J. Kleebe, Microstructure evolution of a W-doped $ZrB_2$ ceramic upon high-temperature oxidation. J. Am. Ceram. Soc. 4 (2017) 1760–1772.
22) L. Silvestroni, H-J. Kleebe, Critical oxidation behavior of Ta-containing $ZrB_2$ composites in the 1500-1650°C temperature range, J. Europ. Ceram. Soc. 37 (2017) 1899–1908.
23) W.G. Fahrenholtz, E.J. Wuchina, W.E. Lee, Y. Zhou, Ultra-High Temperature Ceramics: Materials for Extreme Environment Applications, Wiley & Sons Inc., Hoboken, New Jersey, 2014.
24) D.R.G. Mitchell, DiffTools: Software Tools for Electron Diffraction in Digital Micrograph, Micr. Res. and Technique, 71 (2008) 588-593.
25) L. Silvestroni, D. Sciti, L. Charpentier, M. Balat-Pichelin, Zirconium carbide doped with Tantalum Silicide: microstructure, mechanical properties and high temperature oxidation, Mater. Chem. and Physics, 143 (2013) 407-415.
26) N. Chouard, D. Caurant, O. Majérus, N. Guezi-Hasni, J.-L. Dussossoy, R. Baddour-Hadjean, J.-P. Pereira-Ramas, Thermal stability of $SiO_2$–$B_2O_3$–$Al_2O_3$–$Na_2O$–CaO glasses with high $Nd_2O_3$ and $MoO_3$ concentrations, J. Alloys. Comp. 671 (2016) 84-99.
27) X.H. Zhang, P. Hu, J.C. Han, Structure evolution of $ZrB_2$–SiC during the oxidation in air, J. of Mater. Res. 23 (2008) 1961-1972.
28) A. Klinbumrung, T. Thongtem, S. Thongtem, Characterization of Orthorhombic $\alpha$-$MoO_3$ Microplates Produced by a Microwave Plasma Process, J. of Nanomater. (2012) Article ID 930763, doi:10.1155/2012/930763
29) G.K Bansal, A.H Heuer, On a martensitic phase transformation in zirconia ($ZrO_2$)—I. Metallographic evidence, Acta Metallurgica, 20 (1972) 1281-1289.

30) M. Kazemzadeh Dehdashti, W.G. Fahrenholtz, G.E. Hilmas, Effects of transition metals on the oxidation behavior of $ZrB_2$ ceramics, Corros. Sci. 91 (2015) 224–231.
31) J. B. Berkowitz-Mattuck, 'High Temperature Oxidation. III. Zirconium and Hafnium Diborides, J. Electrochem. Soc. 113 (1966) 908–14.
32) E. A. Gulbransen, K. F. Andrew, and F. A. Brassart, Oxidation of Molybdenum 550° to 1700°C, J. Electrochem. Soc. 110 (1963) 952-959.
33) M.M. Opeka, I.G. Talmy, J.A. Zaykoski, Oxidation-based materials selection for 2000°C + hypersonic aerosurfaces: theoretical considerations and historical experience, J. Mater. Sci. 39 (2004) 5887–5904.
34) K. Shugart, S. Liu, F. Craven, E. Opila, Determination of retained $B_2O_3$ content in $ZrB_2$-30 vol% SiC oxide scales, J. Am. Ceram. Soc. 98 (2015) 287–295.
35) J. J. Ramos-Hernandez, J. Porcayo-Calderon, V. M. Salinas-Bravo, C. D. Arrieta-Gonzalez, J. G. Gonzalez-Rodriguez, L. Martinez-Gomez, Phase Stability Diagrams for High Temperature Corrosion Processes, Mathematical Problems in Engineering, (2013) Article ID 542061, 7 pages, doi:10.1155/2013/542061.
36) W.G. Fahrenholtz, The $ZrB_2$ Volatility Diagram, J. Am. Ceram. Soc. 88 (2005) 3509–3512.
37) J. Han, P. Hu, X. Zhang, S. Meng, Oxidation behavior of zirconium diboride–silicon carbide at 1800°C. Scr. Mater., 57 [9] (2007) 825-828.
38) L. Silvestroni, S. Failla, I. Nehpor, O. Grigoriev, Method to improve the oxidation resistance of $ZrB_2$-based ceramics for reusable space systems, J. Europ. Ceram. Soc. 38 (2018) 2467–2476.
39) M. Taya, S. Hayashi, A.S. Kobayashi, H.S. Yoon, Toughening of a Particulate Ceramic-Matrix Composite by Thermal Residual Stress, J. Am. Ceram. Soc. 73 (1990) 1382–1391.
40) M. Gulbrasen, E.A. Gulbransen, K.F. Andrew, F.A. Brassart, Kinetics of oxidation of pure tungsten, 1150°–1615°C, J Electrochem. Soc. 111 (1964) 103–109.
41) S.P. Garg, N. Krishnamurthy, A. Awasthi, M. Venkatraman, The O-Ta(Oxygen-Tantalum) system, J. Phase Equil. 17 (1996) 63–77.
42) R. Speiser, G.R. St. Pierre, Fundamentals of refractory metal-gaseous environmental interaction, in: N E Promisel (Ed.), The Science and Technology of Tungsten,Tantalum, Molybdenum, Niobium and Their Alloys, Pergamon Press, NewYork, 1964, pp. 289–330.
43) I.G. Talmy, J.A. Zaykoski, M.M. Opeka, High-Temperature Chemistry and Oxidation of $ZrB_2$ Ceramics Containing SiC, $Si_3N_4$, $Ta_5Si_3$, and $TaSi_2$, J. Am. Ceram. Soc. 91 (2008) 2250–2257.
44) J. Watts, G.E. Hilmas, W.G. Fahrenholtz, D. Brown, B. Clausen, Measurement of thermal residual stresses in $ZrB_2$ –SiC composites, J. Europ. Ceram. Soc. 31 (2011) 1811–20.

**Figures captions**

Fig. 1: a)-b) SEM images showing the overall microstructure with secondary phases, c)-d) BF-TEM images of the matrix core-rim sub-structure with dislocation networks in the rim and corresponding e) diffraction patterns showing epitaxy and f) EDS spectra. g) $SiO_2$ precipitates trapped at the core-rim interface.

Fig. 2: a) BF-TEM image of a $SiO_2$ pocket with precipitates trapped into $ZrB_2$ grains, b) magnified view of the boxed area in a) with EDS spectra of $ZrO_2$ precipitates dispersed into the $SiO_2$ glass and c) corresponding diffraction patterns.

Fig. 3: X-ray diffraction spectra of the $ZrB_2$-$MoSi_2$ ceramic upon oxidation at a) 1650°C and b) 1800°C for 15 minutes.

Fig. 4: SEM images showing the microstructural features of the external surface of the $ZrB_2$-$MoSi_2$ ceramic upon oxidation at a)-c) 1650°C and d)-f) 1800°C for 15 minutes with EDS spectra of the phases indicated. The inset in d) is an overview of the oxidized bar at 1800°C.

Fig. 5: SEM image of the polished cross section of the $ZrB_2$-$MoSi_2$ ceramic upon oxidation 1650°C showing an overview of the oxidized scales with elemental maps.

Fig. 6: TEM image of $ZrO_2$ grains within layer I in the ceramic oxidized at 1650°C showing a)-b) an overview of the grains with lamellae and MoB nano-inclusions, c)-e) magnified views of such inclusions with f) diffraction patterns and EDS spectra of $ZrO_2$ and MoB.

Fig. 7: Layer II in the ceramic oxidized at 1650°C showing a) the distribution of the secondary phases in a SEM image, b) TEM image of the MoB phase with c) corresponding EDS spectrum and diffraction pattern, d)-e) $MoO_x$ amorphous phase found at the layer I/layer II interface with f) EDS spectrum and diffraction pattern.

Fig. 8: SEM image of the polished cross section of the $ZrB_2$-$MoSi_2$ ceramic upon oxidation 1800°C showing an overview of the oxidized scales with elemental maps.

Fig. 9: Layer I in the ceramic oxidized at 1800°C showing a) the distribution of the secondary phases in a SEM image at the layerI/layer II interface, b) a magnified view of the boxed area in a) evidencing decreasing precipitates content at the glassy $SiO_2$/solid structure interface and the dendritic growth of $ZrO_2$ indicated

by arrow. c) TEM image of the $SiO_2$-$ZrO_2$ scale in layer I with variable size and concentration of $ZrO_2$ precipitates with EDS spectrum (inset) of the glass and magnified view of the boxed area in d).

Fig. 10: Layer II in the ceramic oxidized at 1800°C showing a) the two types of columnar and globular $ZrO_2$, b) the distribution of MoB nano-inclusions on the $ZrO_2$ grains indicated by arrows and c)-d) cracks originating from such inclusions all across layer II with EDS spectrum of the intergranular glass (inset in c)).

Fig. 11: BF-TEM images of the bulk zone upon oxidation at 1800°C for 15 minutes showing well faceted hexagonal grains of $ZrB_2$, $MoSi_2$ and $SiO_2$.

Fig. 12: Left - Sketch of the microstructure evolution from a) the as-sintered state up to oxidation at b) 1650 and c) 1800°C. Right - phase stability diagrams for the Zr-B-O (black) and Mo-B-O (red) system as a function of oxygen and boron oxide partial pressures calculated at b) 1650°C and c) 1850°C. The shaded areas define partial pressure conditions established from the outer surface and across the oxidized scale.

Fig. 13: (a) Transition metals selected as possible dopants for $ZrB_2$ to form $(Zr,Me)B_2$ upon densification and (b) nature of the nano-inclusions trapped in $ZrO_2$ predicted to form upon oxidation at 1650°C at $PO_2$ below $10^{-13}$ atm and $PB_2O_3$ below $10^{-2}$ atm. Detailed predominance diagrams are reported in Fig. S1.

**SUPPLEMENTARY INFORMATION**

**Appendix 1**

In this appendix, the equations used for calculating the residual stress in $ZrO_2$ grains, $\sigma_m$, due to the inclusion of nano-particles of either MoB, W or $TaB_2$ are reported. In this first approximation, the input data are reported in Table II.

$$\sigma_m = E_m \frac{2 f \beta \varepsilon^*}{(1-f)(\beta+2)(1+\nu_m)+3\beta f(1-\nu_m)} \quad (7)$$

where $E_m$ *is* Young's modulus of the matrix*, f* is the nano-inclusions volumetric fraction and $\beta$ is given by:

$$\beta = \frac{1+\nu_m}{1-2\nu_p}\frac{E_p}{E_m} \quad (8)$$

$E_p$, $\nu_p$ and $\nu_m$ are Young's modulus and Poisson ratio of particles and matrix, respectively, and $\varepsilon^*$ is the thermal expansion misfit strain given by:

$$\varepsilon^* = (\alpha_p - \alpha_m)\Delta T \quad (9)$$

where the $\alpha_p$, $\alpha_m$ are the thermal expansion coefficients of reinforcement and matrix, respectively and $\Delta T$ is the temperature at which stresses begin to accumulate, set as 1400°C [44].

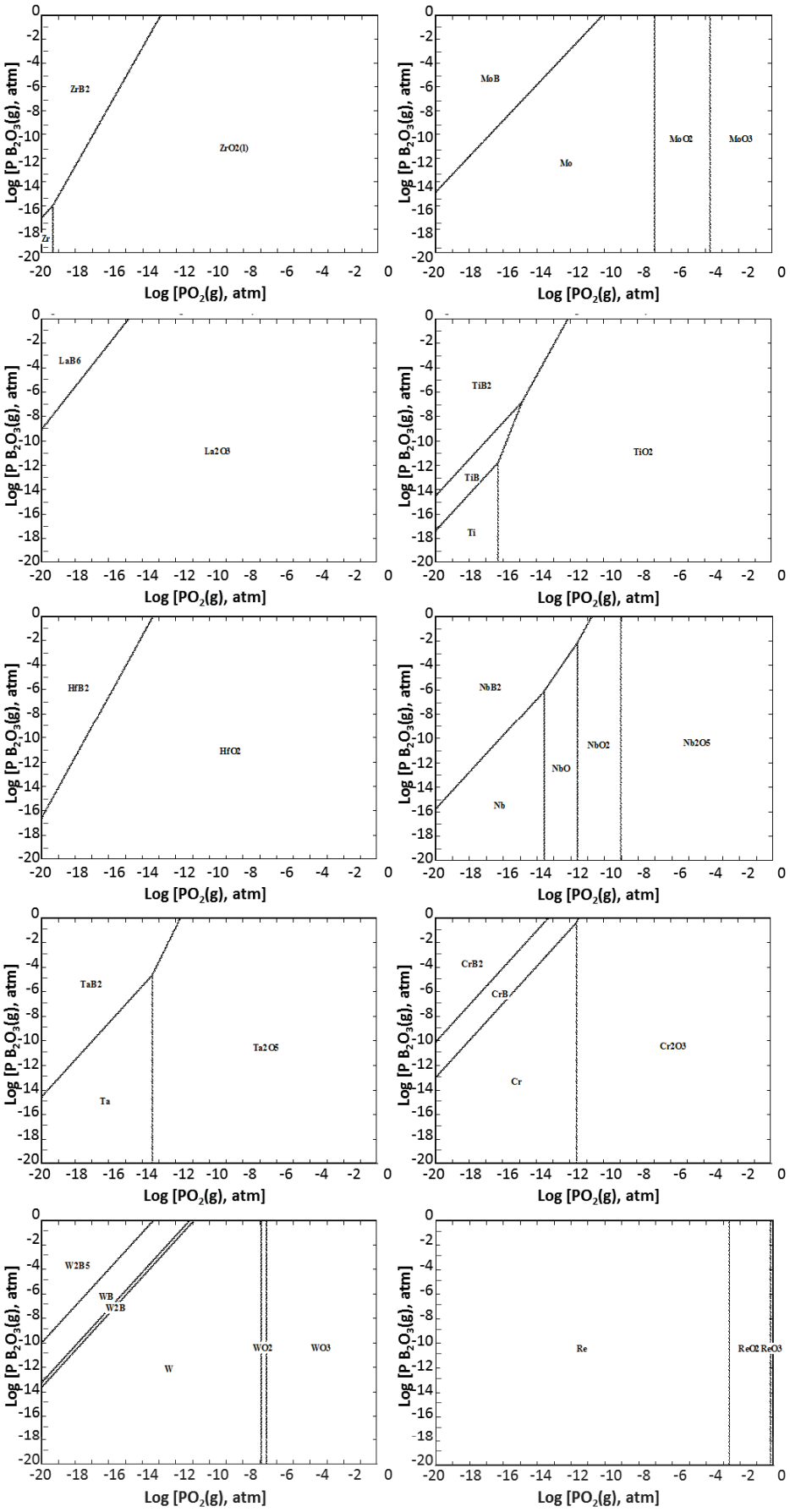


**Fig. S1:** Computed phase stability diagrams for various Me-B-O systems at 1650°C as a function of oxygen and boron oxide partial pressures.

**Figure 1**
Click here to download high resolution image

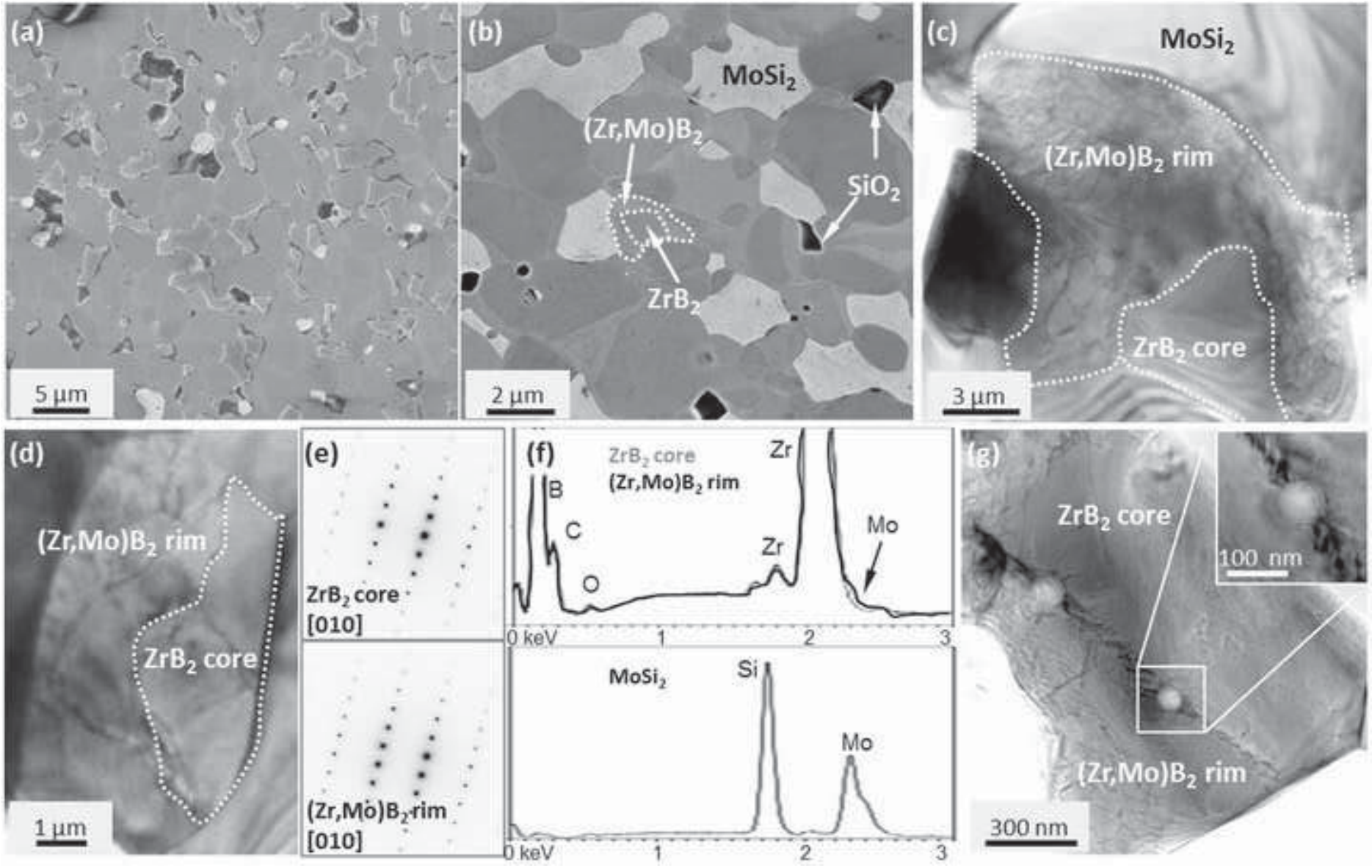

**Figure 2**
Click here to download high resolution image

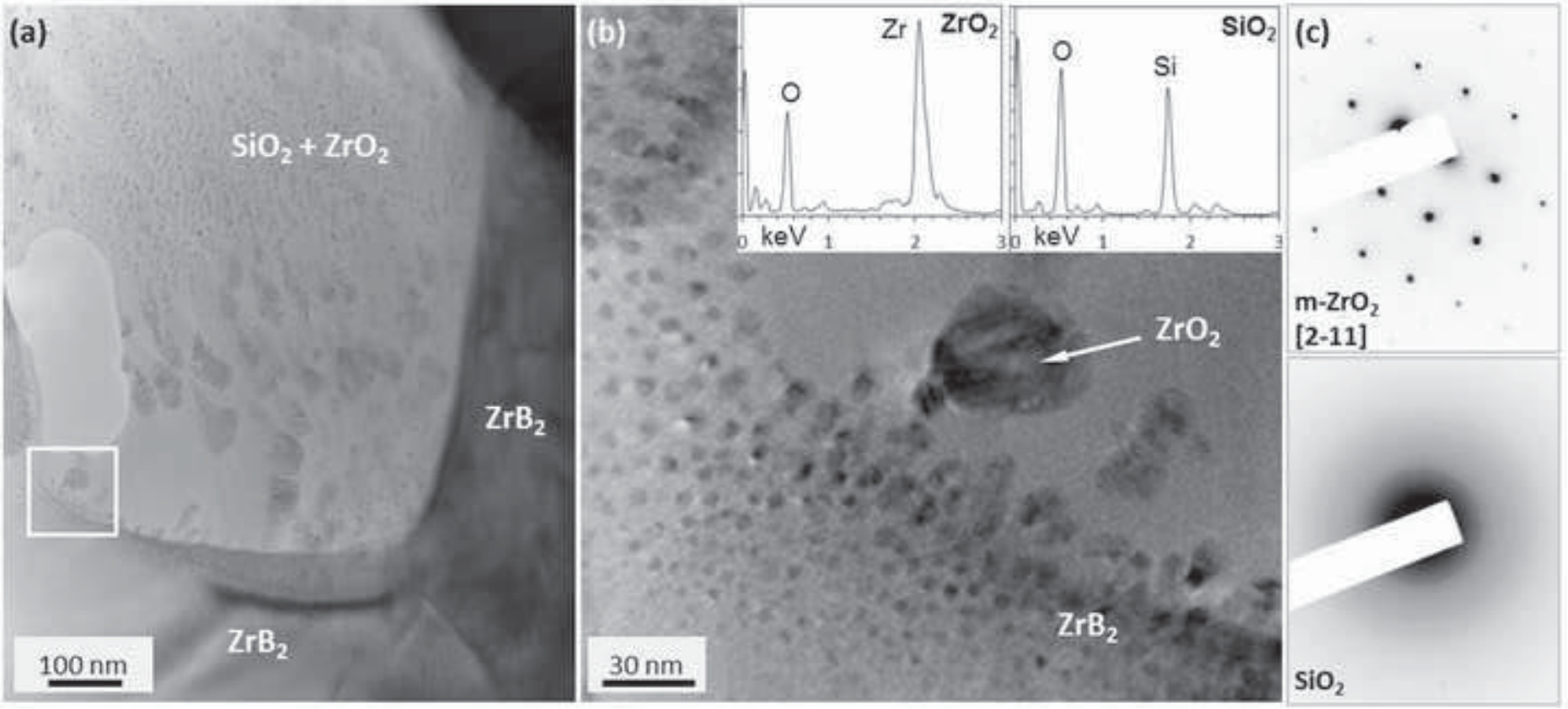

**Figure 3**

Click here to download high resolution image

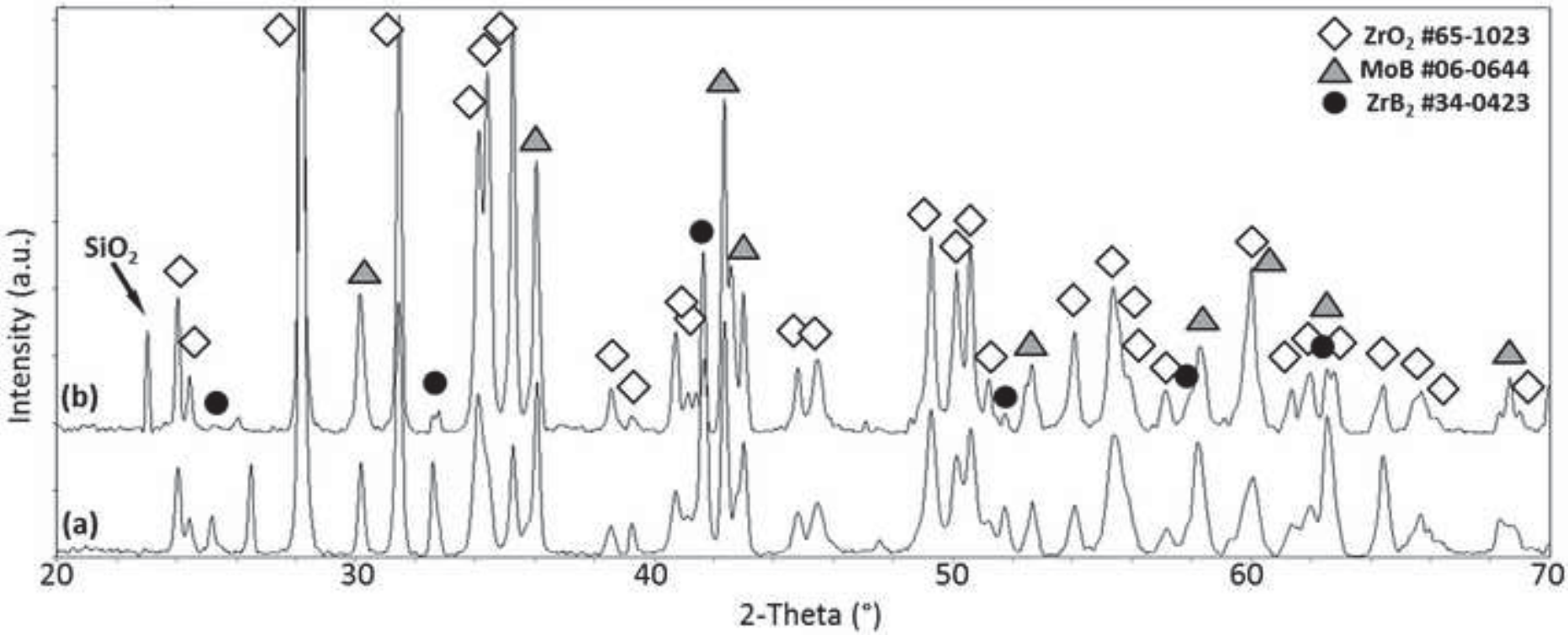

Figure 4
Click here to download high resolution image

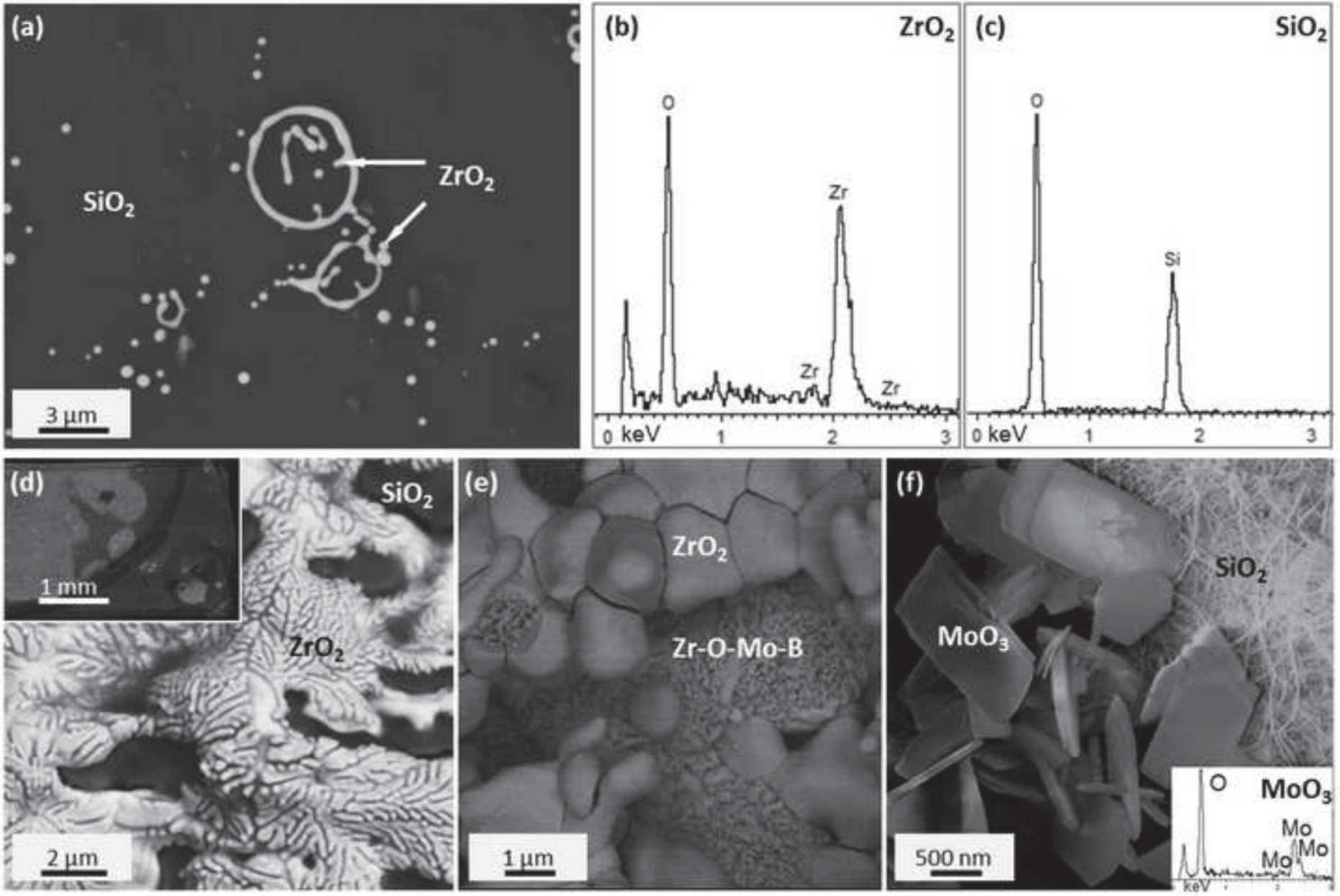

**Figure 5**

Click here to download high resolution image

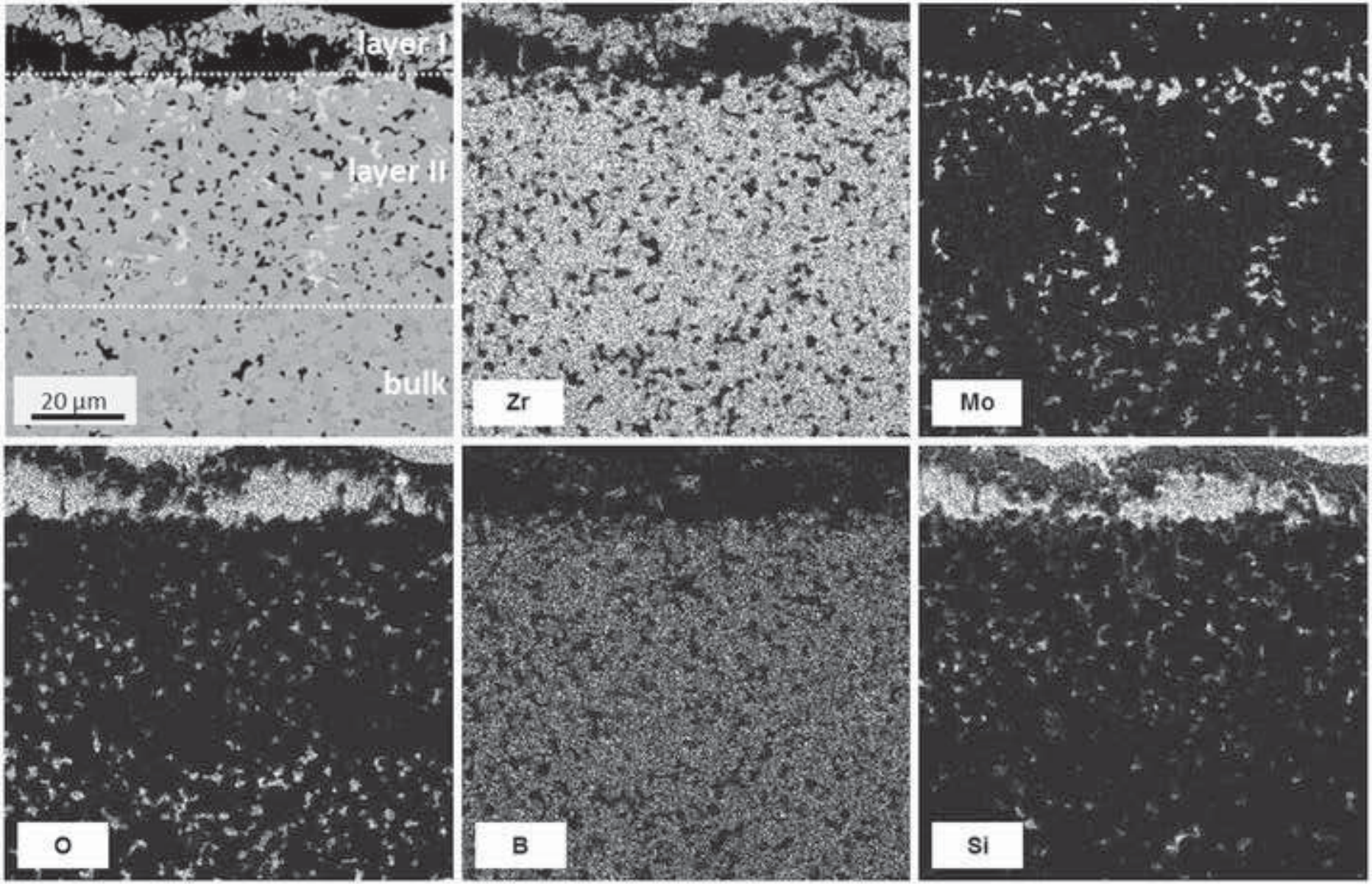

**Figure 6**

Click here to download high resolution image

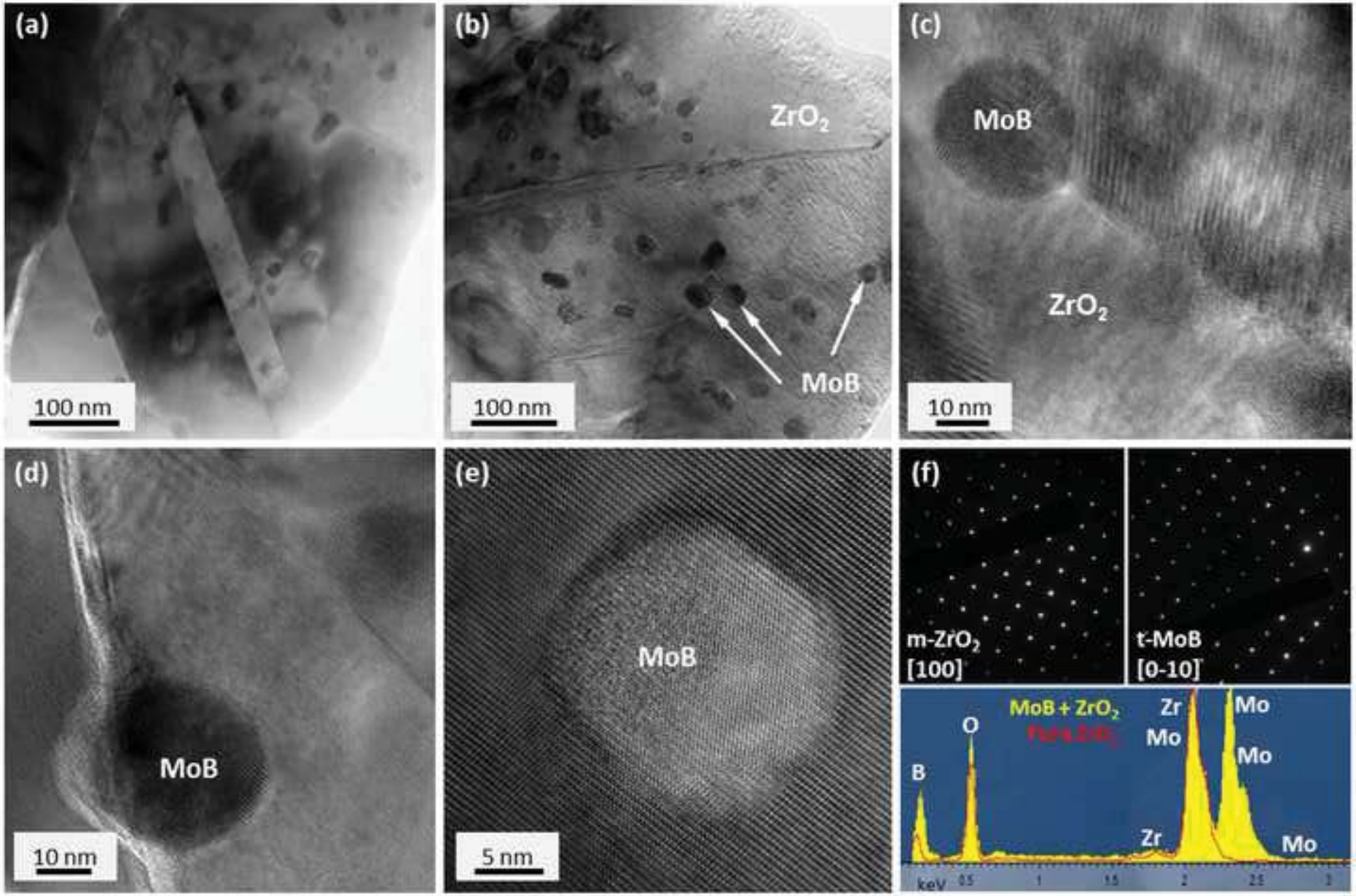

Figure 7
Click here to download high resolution image

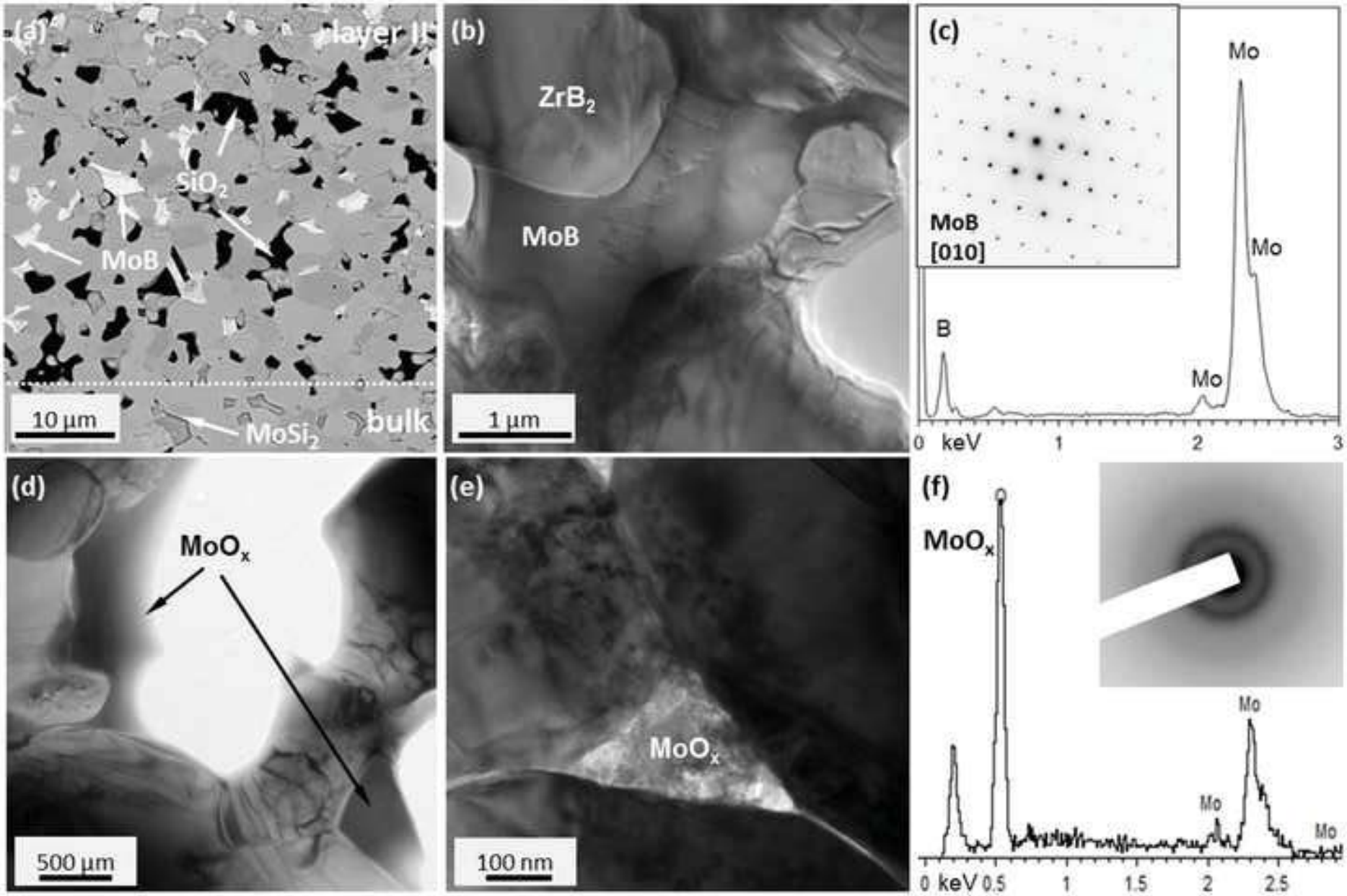

**Figure 8**

Click here to download high resolution image

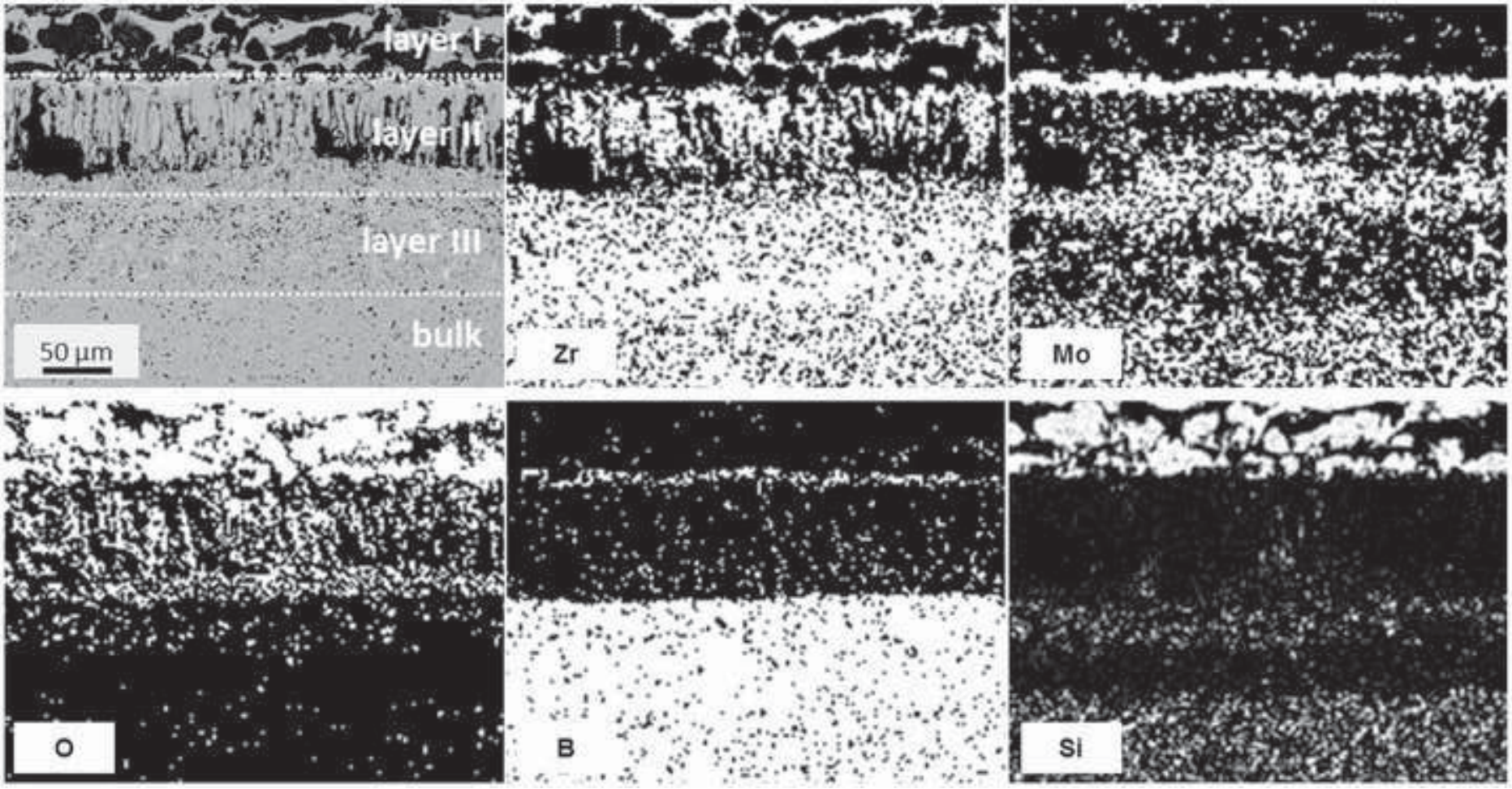

**Figure 9**

Click here to download high resolution image

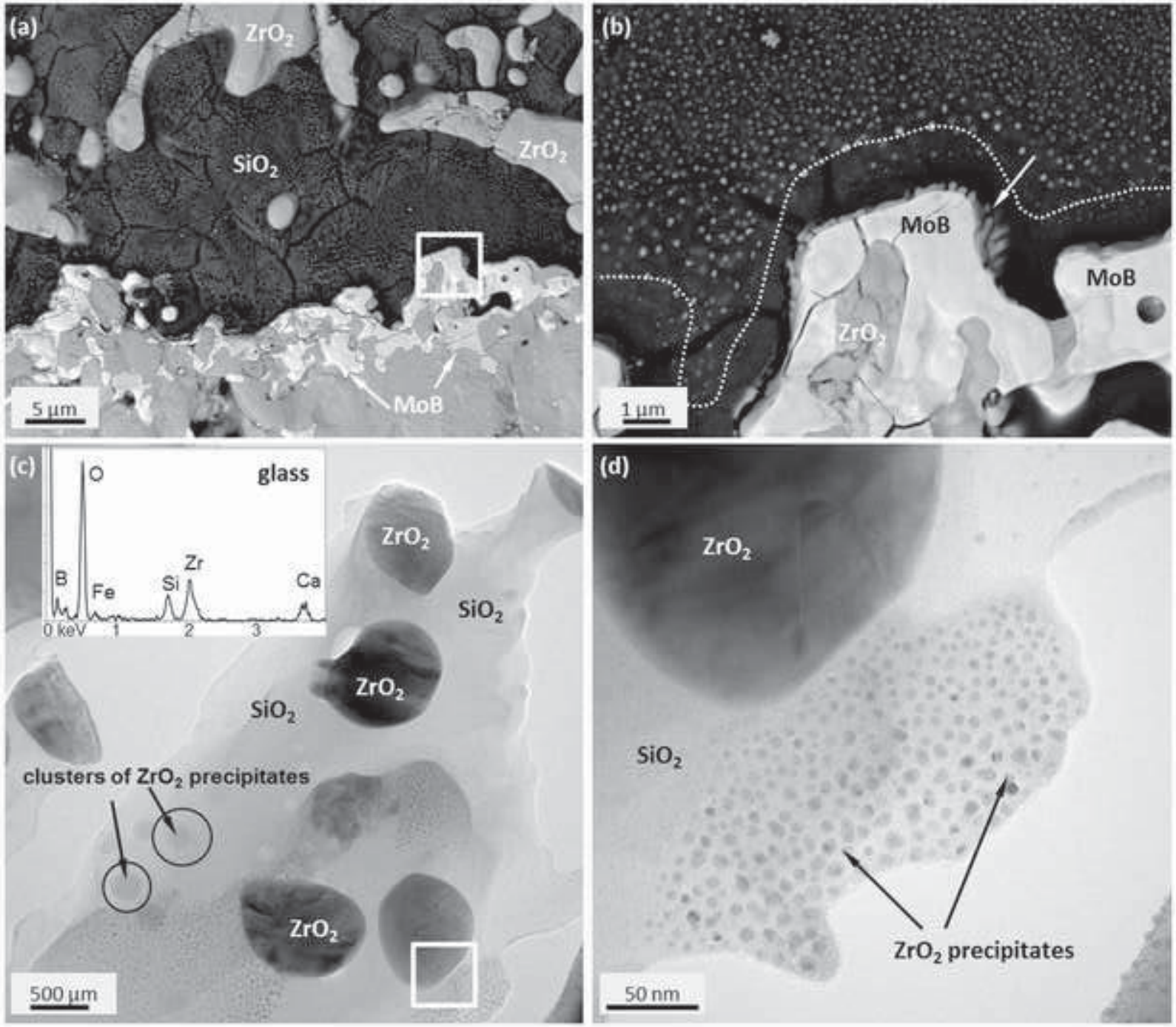

**Figure 10**

Click here to download high resolution image

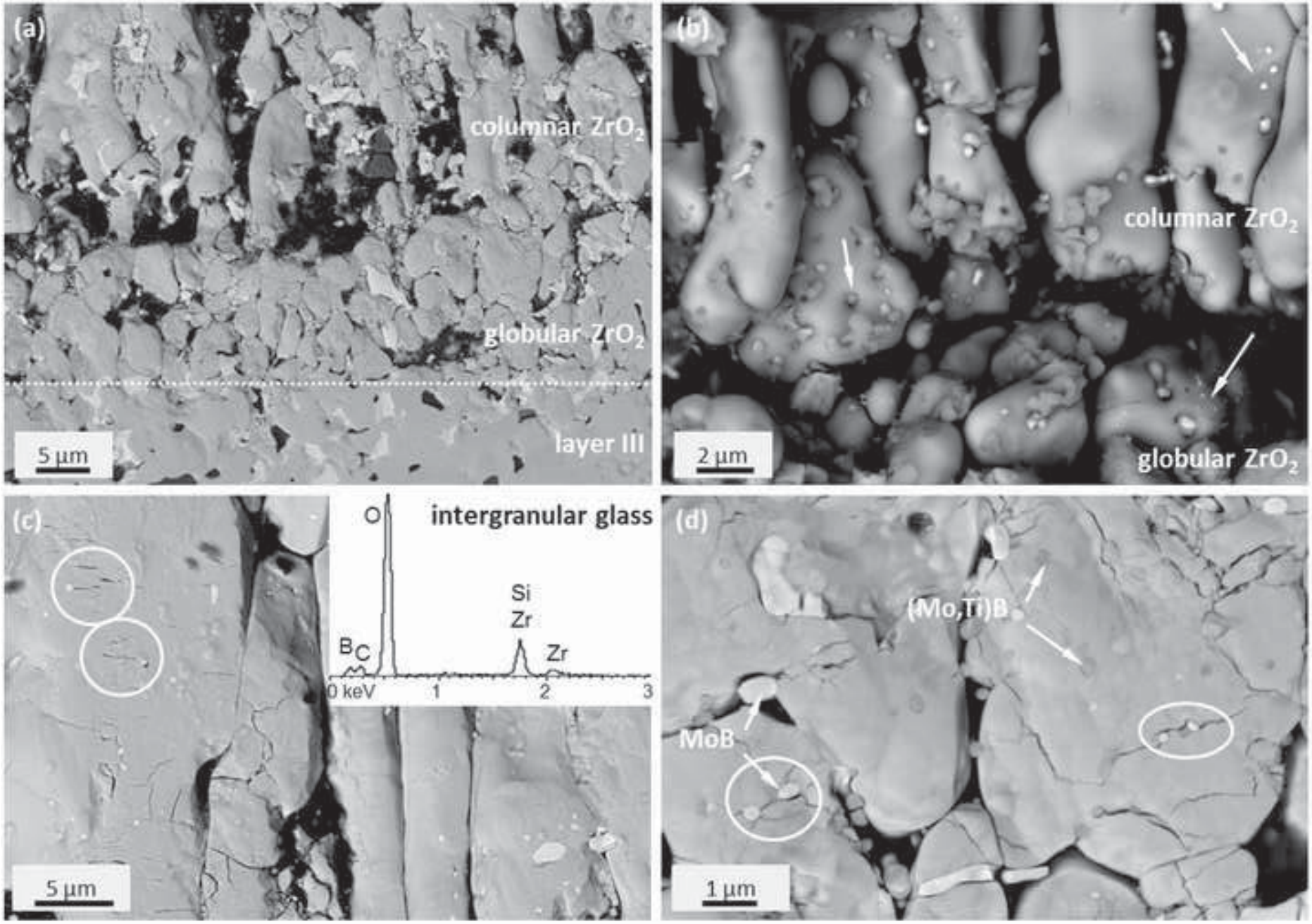

**Figure 11**

Click here to download high resolution image

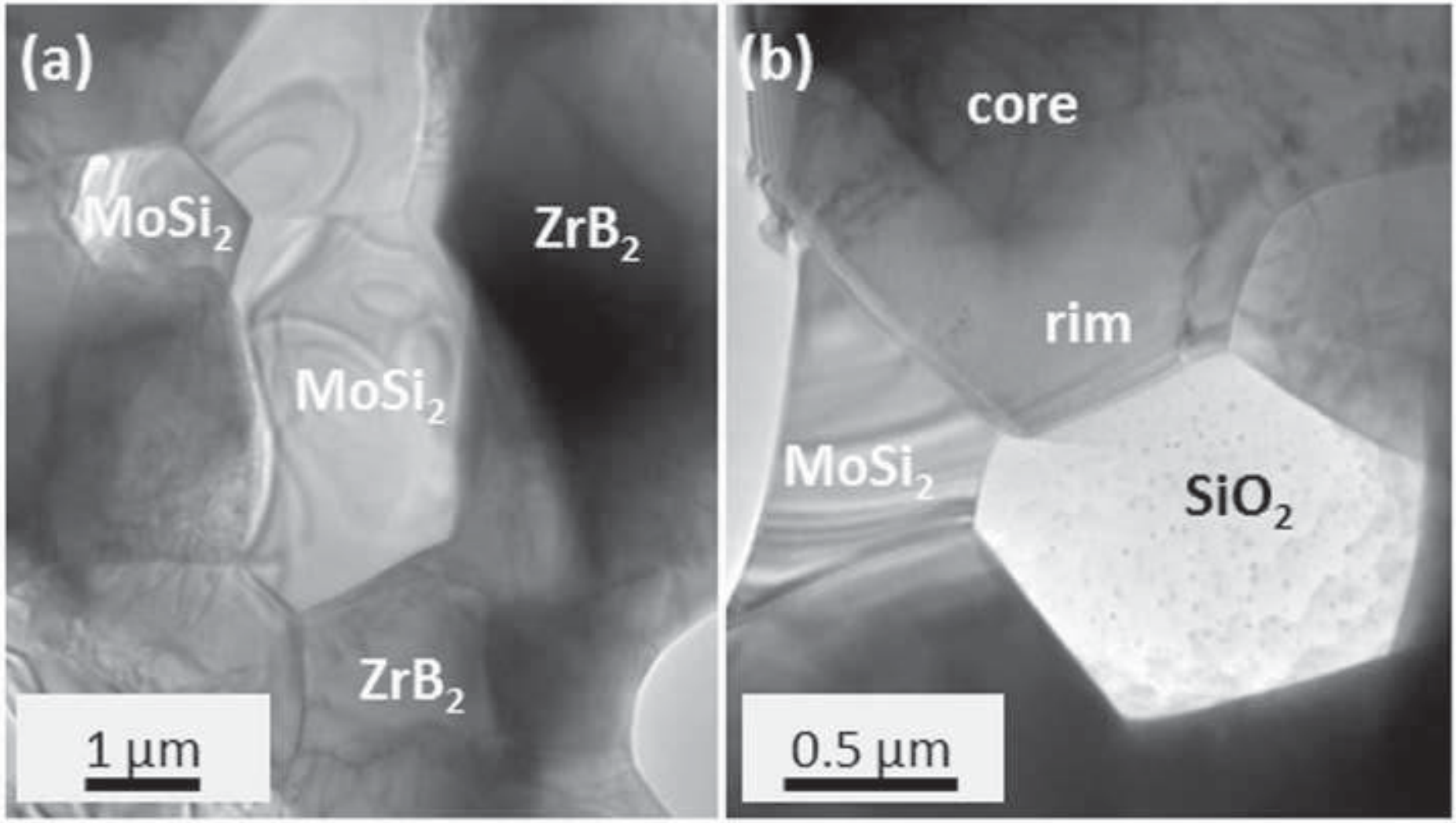

Figure 13
Click here to download high resolution image

(a)

| | | | | |
|---|---|---|---|---|
| Sc | Ti | V | Cr | Mn |
| Y | Zr | Nb | Mo | Tc |
| La | Hf | Ta | W | Re |

(b)

| | | | | |
|---|---|---|---|---|
| Sc | $TiB_2/TiO_2$ | V | Cr | Mn |
| Y | $ZrO_2$ | $NbB_2$ | MoB | Tc |
| $La_2O_3$ | $HfB_2/HfO_2$ | $TaB_2$ | W | Re |

**Figure 12**
**Click here to download high resolution image**

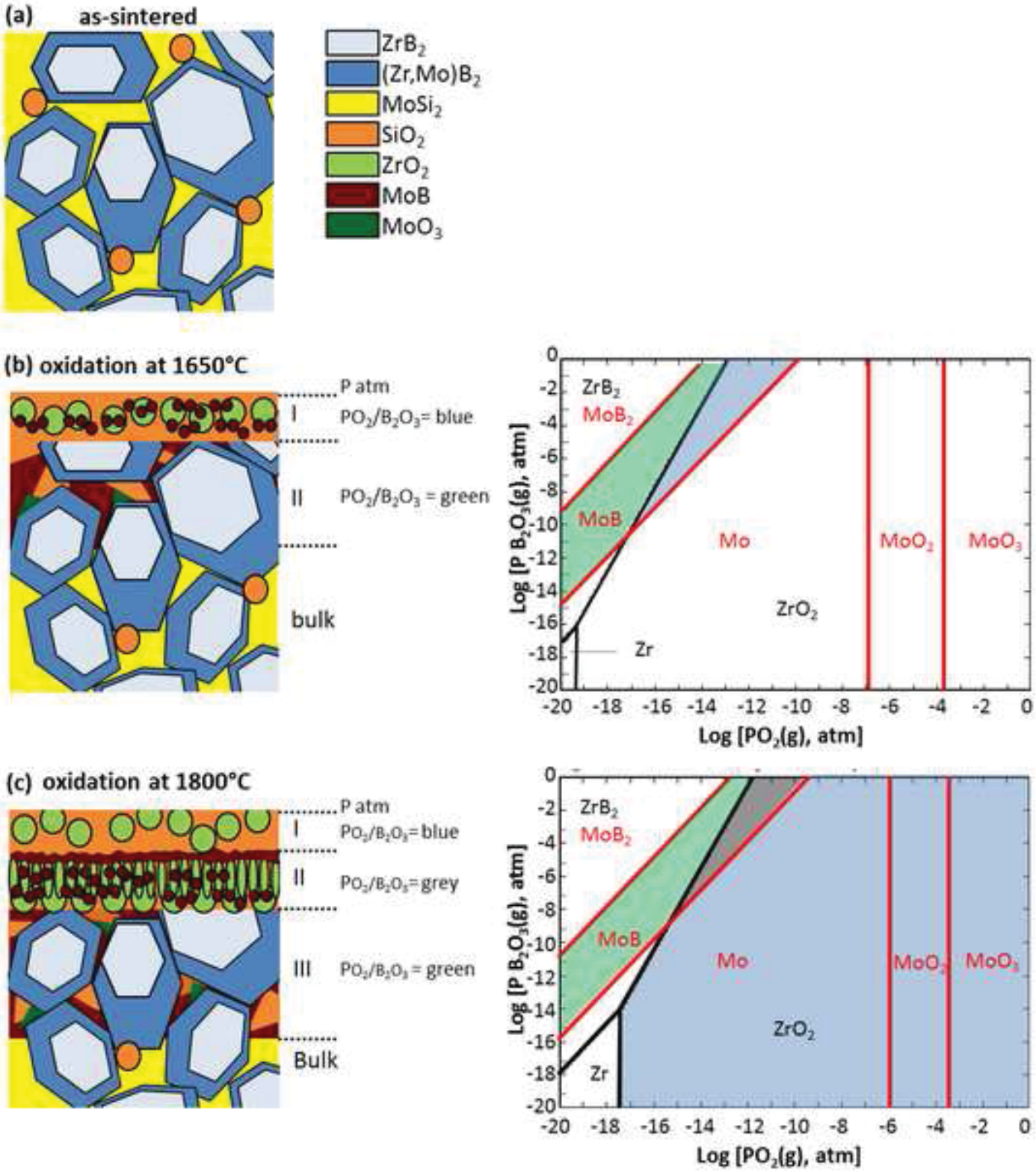

**Table(s)**

## Tables

**Table I:** Composition and main microstructural features of the as-sintered and oxidized $ZrB_2$–$MoSi_2$ composite.

| **$ZrB_2$-$MoSi_2$** | **Phase composition** | **µm** |
|---|---|---|
| **as-sintered** | $(Zr,Mo)B_2$, $ZrB_2$, $MoSi_2$, $SiO_2$, $ZrO_2$, MoB | bulk |
| **ox 1650°C** | layer I: $SiO_2$, $ZrO_2$ + MoB incl | 15±3 |
| | layer II: $(Zr,Mo)B_2$, $ZrB_2$, $SiO_2$, MoB, am $MoO_3$ | 50±4 |
| **ox 1800°C** | layer I: $SiO_2$, $ZrO_2$, $MoO_{3(s)}$ | 50±5 |
| | layer II: MoB, $SiO_2$, $ZrO_2$ + MoB incl | 85±5 |
| | layer III: $(Zr,Mo)B_2$, $ZrB_2$, $SiO_2$, MoB, am $MoO_3$ | 45±5 |

**Table II:** Collection of microstructure details of $ZrB_2$ composites containing initial 15 vol% of $MoSi_2$ (ZBM), $WSi_2$ (ZBW) and $TaSi_2$ (ZBT) being oxidized at 1650°C for 15 minutes [21,22] and properties of the resulting oxidation products. $ZrO_2$ properties are also reported in brackets for comparison. CTE: coefficient of thermal expansion, E: Young's modulus, $\nu$: Poisson's coefficient.

| | | **ZBM** | **ZBW** | **ZBT** |
|---|---|---|---|---|
| Experimental evidence on $ZrB_2$-$MeSi_2$ | Initial Me in $(Zr,Me)B_2$ ss, at% | 5 | 2 | 20 |
| | Me atomic radius, nm (Zr=0.160) | 0.136 | 0.137 | 0.143 |
| Oxidation products properties | Inclusion nature | MoB | W | $TaB_2$ |
| | Inclusion radius, nm | 20 | 15 | 140 |
| | Inclusion CTE ($ZrO_2$: 8.7-10.3) | 7.2 | 4.5 | 8.2 |
| | Inclusion E ($ZrO_2$: 200 GPa) | - | 411 | 560 |
| | $\nu$ ($ZrO_2$: 0.22) | - | 0.28 | 0.22 |
| | Inclusion oxidation product | $MoO_3$ | $WO_3$ | $Ta_2O_5$ |
| | $\Delta$Vol% from boride to oxide | +20 | +64 | +50 |
| | Oxide volatilization T,°C | >1200 | >1150 | >1800 |